

## THE EINSTEIN CROSS: CONSTRAINT ON DARK MATTER FROM STELLAR DYNAMICS AND GRAVITATIONAL LENSING

GLENN VAN DE VEN<sup>1,2</sup>, JESÚS FALCÓN-BARROSO<sup>3,4</sup>, RICHARD M. McDERMID<sup>5</sup>, MICHELE CAPPELLARI<sup>6</sup>, BRYAN W. MILLER<sup>7</sup>, P. TIM DE ZEEUW<sup>8,9</sup>

*Draft version May 29, 2018*

### ABSTRACT

We present two-dimensional line-of-sight stellar kinematics of the lens galaxy in the Einstein Cross, obtained with the GEMINI 8m telescope, using the GMOS integral-field spectrograph. The stellar kinematics extend to a radius of  $4''$  (with  $0.2''$  spaxels), covering about two-thirds of the effective (or half-light) radius  $R_e \simeq 6''$  of this early-type spiral galaxy at redshift  $z_l \simeq 0.04$ , of which the bulge is lensing a background quasar at redshift  $z_s \simeq 1.7$ . The velocity map shows regular rotation up to  $\sim 100 \text{ km s}^{-1}$  around the minor axis of the bulge, consistent with axisymmetry. The velocity dispersion map shows a weak gradient increasing towards a central ( $R < 1''$ ) value of  $\sigma_0 = 170 \pm 9 \text{ km s}^{-1}$ . We deproject the observed surface brightness from HST imaging to obtain a realistic luminosity density of the lens galaxy, which in turn is used to build axisymmetric dynamical models that fit the observed kinematic maps. We also construct a gravitational lens model that accurately fits the positions and relative fluxes of the four quasar images. We combine these independent constraints from stellar dynamics and gravitational lensing to study the total mass distribution in the inner parts of the lens galaxy.

We find that the resulting luminous and total mass distribution are nearly identical around the Einstein radius  $R_E = 0.89''$ , with a slope that is close to isothermal, but which becomes shallower towards the center if indeed mass follows light. The dynamical model fits to the observed kinematic maps result in a total mass-to-light ratio  $\Upsilon_{\text{dyn}} = 3.7 \pm 0.5 \Upsilon_{\odot,I}$  (in the  $I$ -band). This is consistent with the Einstein mass  $M_E = 1.54 \times 10^{10} M_{\odot}$  divided by the (projected) luminosity within  $R_E$ , which yields a total mass-to-light ratio of  $\Upsilon_E = 3.4 \Upsilon_{\odot,I}$ , with an error of at most a few per cent. We estimate from stellar populations model fits to colors of the lens galaxy a stellar mass-to-light ratio  $\Upsilon_{\star}$  from 2.8 to  $4.1 \Upsilon_{\odot,I}$ . Although a *constant* dark matter fraction of 20 per cent is not excluded, dark matter may play no significant role in the bulge of this  $\sim L_{\star}$  early-type spiral galaxy.

*Subject headings:* gravitational lensing — stellar dynamics — galaxies: photometry — galaxies: kinematics and dynamics — galaxies: structure

### 1. INTRODUCTION

In the cold dark matter (CDM) paradigm for galaxy formation (e.g. Kauffmann & van den Bosch 2002), galaxies are embedded in extended dark matter distributions with a specific and (nearly) universal radial profile (e.g. Navarro et al. 1997; Merritt et al. 2005). Measurements of rotation curves from neutral hydrogen (H I) observations in the outer parts of late-type galaxies have provided evidence for the presence of dark matter in these systems already more than two decades ago (e.g. van Albada et al. 1985). In the outer parts of early-type galaxies, however, cold gas is

scarce (but see e.g. Franx et al. 1994; Morganti et al. 1997; Weijmans et al. 2008), so evidence for a dark matter halo has to come from other tracers, such as kinematics of stars, planetary nebulae and globular clusters (e.g. Carollo et al. 1995; Gerhard et al. 2001; Romanowsky et al. 2003; Côté et al. 2003) or hot X-ray gas (e.g. Fukazawa et al. 2006; Humphrey & Buote 2010). However, these tracers are not always (sufficiently) available, the observations are often challenging, and the interpretation modeling dependent. Also in the inner parts of galaxies the amount, shape and profile of dark matter is still poorly known (e.g. Primack 2004), even though stellar kinematics are readily available.

A fundamental problem in using stellar kinematics (as well as other collisionless kinematic tracers) for this purpose is the mass-anisotropy degeneracy: a change in the measured line-of-sight velocity dispersion can be due to a change in total mass, but also due to a change in velocity anisotropy. Both effects can be disentangled by measuring also the higher-order velocity moments (Dejonghe 1987; van der Marel & Franx 1993; Gerhard 1993), but only the inner parts of nearby galaxies are bright enough to obtain the required high-quality kinematic measurements (e.g. van der Marel 1991; Gerhard et al. 2001; Cappellari et al. 2006). A unique alternative to break the mass-anisotropy degeneracy is provided by gravitational lensing. In case of strong lensing, the mass of a

<sup>1</sup> Max Planck Institute for Astronomy, Königstuhl 17, 69117 Heidelberg, Germany: glenn@mpia.de

<sup>2</sup> Institute for Advanced Study, Einstein Drive, Princeton, NJ 08540, USA; Hubble Fellow

<sup>3</sup> Instituto de Astrofísica de Canarias. Vía Láctea s/n, La Laguna. Tenerife. Spain

<sup>4</sup> European Space Agency / ESTEC, Keplerlaan 1, 2200 AG Noordwijk, The Netherlands

<sup>5</sup> Gemini Observatory, 670 N. A'ohoku Place Hilo, Hawaii, 96720, USA

<sup>6</sup> Sub-Department of Astrophysics, University of Oxford, Denys Wilkinson Building, Keble Road, Oxford OX1 3RH, United Kingdom

<sup>7</sup> Gemini Observatory, Casilla 603, La Serena, Chile

<sup>8</sup> European Southern Observatory, Karl-Schwarzschild Strasse 2, 85748 Garching bei München, Germany

<sup>9</sup> Sterrewacht Leiden, Leiden University, Niels Bohrweg 2, 2333 CA Leiden, The Netherlands

foreground galaxy bends the light of a distant bright object behind it, resulting in multiple images. From the separation and fluxes of the images the total mass distribution of the lens galaxy can be inferred directly. The velocity anisotropy then can be determined from the observed velocity dispersion, without the need for higher-order velocity moments.

Treu & Koopmans (2004, and references therein) have applied this approach to several strong lensing systems, of which 0047-281 (Koopmans & Treu 2003) is the best constrained case, with three radially separated velocity dispersion measurements extending to about the effective radius of the lens galaxy. They measure the mass within the Einstein radius by fitting a singular isothermal ellipsoid to the positions of the quasar images. This Einstein mass is used to set the amplitude of the total (stellar and dark) matter distribution, which they assume to be spherical. The constant stellar mass-to-light ratio  $\Upsilon_*$  determines the contribution of the stars with a fixed radial profile, with the remainder due to dark matter with a single power-law profile with slope  $\gamma$ . They then compare the dispersion profile predicted by the spherical Jeans equations, for an ad-hoc assumption of the velocity anisotropy  $\beta$ , with the observed dispersion measurements. Based on a reasonably constrained  $\Upsilon_*$  and an upper limit on  $\gamma$ , they conclude that a significant amount of dark matter is present in the inner parts of the lens galaxy, with a slope shallower than the nearly isothermal total mass distribution. An additional (external) constraint on  $\Upsilon_*$  (or  $\gamma$ ) is needed to go beyond this limit on the dark matter distribution. Even so, their results are limited by too few kinematic constraints (which leaves the anisotropy degenerate), and by the use of a simple spherical dynamical model.

Clearly, most lens galaxies are significantly flattened and so cannot be well-described by spherical models. Non-spherical models provide a more realistic description of the lens galaxy, but the increase in freedom requires also (significantly) more spatially resolved kinematic measurements to constrain them. Only a few of the known strong gravitational lens systems are close enough to obtain such kinematic data. Even then, one can make (ad-hoc) assumptions on the velocity distribution, such as velocity isotropy in the meridional plane of an axisymmetric model. The latter restriction to a distribution function of two (instead of three) integrals of motion allows for the recovery of the intrinsic shape and mass distribution in the presence of two-dimensional kinematic data (Barnabè & Koopmans 2007; Czoske et al. 2008; Barnabè et al. 2009), possibly even without the additional constraint provided by gravitational lensing (e.g. Cappellari et al. 2006).

In this paper, we relax the two-integral assumption and find that one can still derive independent determinations of the intrinsic mass distribution from both gravitational lensing and stellar dynamics with two-dimensional kinematic data. We have observed the gravitational lens system QSO 2237+0305, well-known as the Einstein Cross, with the integral-field spectrograph GMOS on the GEMINI-North Telescope. We fit the extracted stellar velocity and velocity dispersion maps of the inner parts of the lens galaxy at a redshift  $z_l \simeq 0.04$  with axisymmetric dynamical models. The resulting intrinsic mass distribution agrees well with that inferred from the lens

model that fits the four quasar image positions and relative fluxes. Furthermore, we compare this total mass distribution with the stellar mass distribution, based on an independent estimate of the stellar mass-to-light ratio  $\Upsilon_*$ , to place constraints on the dark matter distribution in the inner parts of the lens galaxy.

In Section 2, we briefly describe the Einstein Cross, and we present the photometric and spectroscopic observations. In Section 3, we extract the two-dimensional stellar kinematics, describe the dynamical modeling method, and construct lens models. From the latter we infer the total mass distribution, which we compare in Section 4 with the luminous mass distribution inferred from the observed surface brightness. We then build axisymmetric dynamical models, and compare the resulting dynamical mass-to-light ratio with that inferred from the lens models, and in turn with an estimate of the stellar mass-to-light ratio. In Section 5 we discuss our findings and we summarize our conclusions.

Throughout we adopt the WMAP cosmological parameters for the Hubble constant, the matter density and the cosmological constant, of respectively  $H_0 = 73 \text{ km s}^{-1} \text{ Mpc}^{-1}$ ,  $\Omega_M = 0.24$  and  $\Omega_L = 0.76$  (WMAP3; Spergel et al. 2007).

## 2. OBSERVATIONS AND DATA REDUCTION

### 2.1. The Einstein Cross

The Einstein Cross is the well-known gravitational lens system QSO 2237+0305 (RA: 22h 40m 30.3s, Dec: +03° 21' 31", J2000). In this system, a distant quasar at redshift  $z_s = 1.695$  is lensed by the bulge of the early-type spiral PGC 069457 at  $z_l = 0.0394$  (angular diameter distance  $D_l = 155 \text{ Mpc}$ ,  $1'' = 0.75 \text{ kpc}$ ), resulting in a cross of four bright images separated by about  $1.8''$ .

The Einstein Cross has long been the closest strong gravitational lens system known, and has been very well studied since its discovery by Huchra et al. (1985). There is a wealth of ground- and space-based imaging data at all wavelengths (e.g. Falco et al. 1996; Blanton et al. 1998; Agol et al. 2000; Dai et al. 2003). The resulting precise measurements of the positions and relative fluxes of the quasar images can be used to construct a detailed lens model.

In contrast, kinematic data of the lens galaxy is very scarce, with only one measured central stellar velocity dispersion (Foltz et al. 1992) and two H I rotation curve measurements in the very outer parts (Barnes et al. 1999). There are several previous integral-field studies of the Einstein Cross: TIGER: Fitte & Adam (1994); INTEGRAL: Mediavilla et al. (1998); CIRPASS: Metcalf et al. (2004). However, none of these studies were concerned with the stellar kinematics of the lens galaxy, but instead investigated the quasar spectra.

### 2.2. Imaging

We use two WFPC2 images retrieved from the HST-archive (F555W *V*-band image, 1600 seconds, PI: Westphal, and F814W *I*-band image, 120 seconds, PI: Kochanek; see left and middle panels of Fig. 1) to determine the luminosity density of the lens galaxy. We correct the *I*-band image for a Galactic extinction of  $E(B - V) = 0.071$  (Schlegel et al. 1998), and we convert to solar units using the WFPC2 calibration of Dolphin

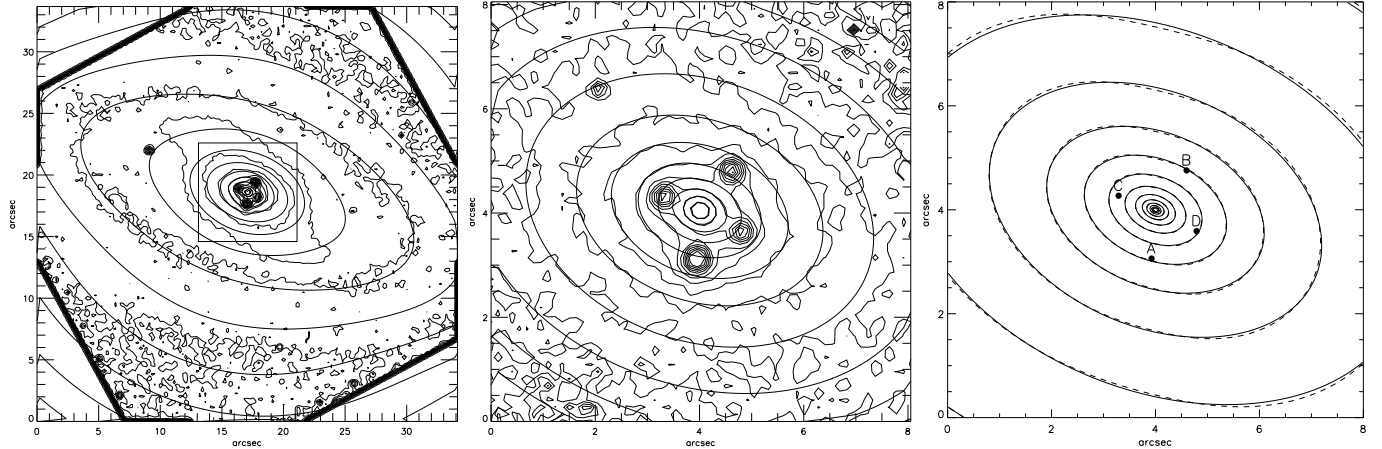


FIG. 1.— Surface brightness as observed with HST (left and middle panel) and surface mass density of the overall best-fit lens model (right panel) of the lens galaxy in the Einstein Cross. *Left panel:* the contours of the WFC2/F555W  $V$ -band image reveal clearly the bulge, spiral arms and bar embedded in the large-scale disk of this early-type spiral galaxy. The ellipticity measured from the MGE fit (contours) is used to estimate the inclination. *Middle panel:* the central  $8'' \times 8''$  of the WFC2/F814W  $I$ -band image, of which the MGE fit is used to construct the (stellar) luminosity density model of the lens galaxy. We use the  $I$ -band image instead of the longer exposed  $V$ -band image as it tracers better the old stellar population and is less sensitive to extinction and reddening. The four quasar images are masked out during the MGE fit. In both WFC2 images the contours are in steps of  $0.5 \text{ mag/arcsec}^2$ . The images are rotated such that North is up and East is to the left. *Right panel:* The scale-free lens model with slope  $\alpha = 1.0$  (dashed contours) fits the positions and relative fluxes of the quasar images, indicated by the filled circles. Superposed is the MGE fit (solid contours).

(2000), while assuming an absolute  $I$ -band magnitude for the Sun of 4.08 mag (Table 2 of Binney & Merrifield 1998). From a de Vaucouleurs  $R^{1/4}$  profile fit to the  $I$ -band photometry in the inner bulge-dominated region, we obtain an effective radius  $R_e \simeq 6''$ , which is consistent with previous measurements (e.g. Racine 1991).

For the construction of the lens model, we use the accurate positions of the quasar images from the website of the CASTLES survey<sup>10</sup> based on *Hubble Space Telescope* (HST) imaging. Although also optical flux ratios are given on this website, we use the radio fluxes provided by Falco et al. (1996), because they are in general (much) less affected by differential extinction or microlensing.

### 2.3. Integral-field spectroscopy

Observations of the Einstein Cross lens system were carried out using the integral-field unit of the GMOS-North spectrograph (Murray et al. 2003; Hook et al. 2004) on July 17<sup>th</sup> and August 1<sup>st</sup> 2005 as part of the program GN-2005A-DD-7; the seeing was about  $0.5''$ . The data were obtained using the IFU two-slit mode that provides a field-of-view of  $5'' \times 7''$ . An array of 1500 hexagonal lenslets, of which 500 are located  $1'$  away from the main field to be used for sky subtraction, sets the  $0.2''$  spatial sampling. Eight individual science exposures of 1895 seconds each were obtained during the two nights, resulting in a total on-source integration time of  $\simeq 4$  hours. An offset of  $0.3''$  was introduced between exposures to avoid bad CCD regions or lost fibers. The R400-G5305 grating in combination with the CaT-G0309 filter was used to cover a wavelength range of 7800–9200 Å with a FWHM spectral resolution of 2.8 Å.

For the data reduction we used an updated version of the officially distributed Gemini IRAF<sup>11</sup> package. We ap-

plied bias subtraction, flat-fielding and cosmic ray rejection (using the *L.A. Cosmic* algorithm by van Dokkum 2001) to each science exposure, and wavelength calibration after the extraction of the data. A careful flat-fielding procedure, crucial for proper removal of fringes in the spectral direction, was carried out using the Quartz halogen (QH) lamp. Wavelength calibration was performed with CuAr lamp exposures taken before each science exposure. At the observed wavelengths, a complex spectrum of  $\text{H}_2\text{O}$  absorption features overlaps with the CaT lines we are interested in. We constructed a correction spectrum from observations of the white dwarf star Wolf1346, taken with the same instrumental setup as our science frames. We checked the range of fiber-to-fiber variations of the spectral resolution of the instrument by measuring the width of the sky lines in each fiber, resulting in the nominal FWHM value of  $2.8 \pm 0.2 \text{ \AA}$  for most of the data cubes. In order to combine all the data, we homogenized the science frames by convolving all spectra to an instrumental FWHM resolution of 3.1 Å (or  $\sigma_{\text{instr}} \simeq 44.2 \text{ km s}^{-1}$ ) and resampling the spectra to the same range and sampling in wavelength. After interpolating each science frame to a common spatial grid, taking into account the small spatial offsets applied during the observations, we sum the spectra sharing the same position in the sky to produce the final merged data cube.

The significant contribution from the sky lines to the overall spectrum of the lens galaxy made the sky subtraction the most challenging step in the data reduction process. Although the scatter in the instrumental resolution was small within the individual science frames, the combined effect of other steps in the data reduction (e.g. fringing, telluric absorption, resampling of data in wavelength), introduced alterations in the shape of the sky lines (from the sky fibers) that were not equally reproduced in the science fibers. As a consequence any attempt to use the sky from the sky fibers resulted in serious systematic effects (i.e. P-Cygni like residuals) in the galaxy spectra underneath. In order to minimize

<sup>10</sup> <http://cfa-www.harvard.edu/castles/>

<sup>11</sup> IRAF is distributed by the National Optical Astronomy Observatories, which are operated by the Association of Universities for Research in Astronomy, Inc., under cooperative agreement with the National Science Foundation.

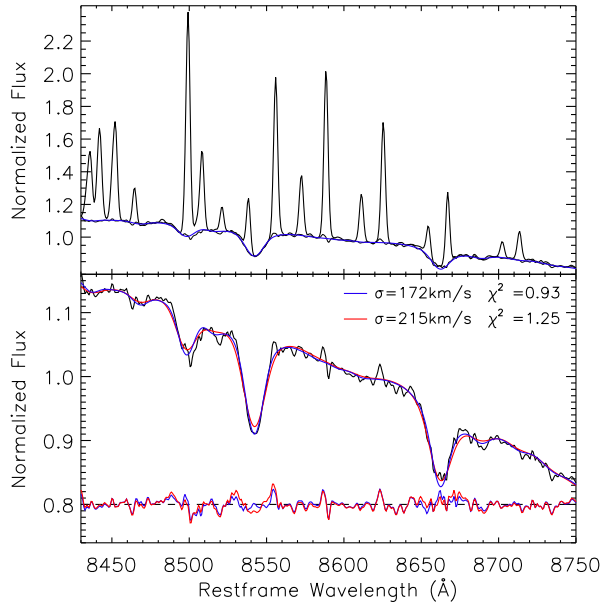


FIG. 2.— Spectrum from the center of the lens galaxy. *Upper panel:* The observed spectrum (thick black curve) clearly shows the contamination by the sky emission lines. The sky-subtracted galaxy spectrum (thin black curve) shows the Ca II triplet absorption lines which are nicely fitted by a composite of stellar population models (blue curve). *Lower panel:* The same sky-subtracted galaxy spectrum (black curve) and composite stellar population model (blue curve) are shown. In addition to the this model with a best-fit velocity dispersion of  $172 \text{ km s}^{-1}$ , another model (red curve) is shown with the velocity dispersion fixed to the  $215 \text{ km s}^{-1}$  as measured by Foltz et al. (1992). The residuals at the bottom and the quoted reduced  $\chi^2$ -values show that  $172 \text{ km s}^{-1}$  provides a better fit than  $215 \text{ km s}^{-1}$ , particularly in fitting the strongest of the three absorption lines. Note that this spectrum is extracted from the same central aperture of  $0.7'' \times 0.4''$  (at a position angle of  $39^\circ$ ) as used by Foltz et al. (1992), and that the seeing conditions were similar. Throughout we use instead a circular aperture with radius  $1''$  to derive the central velocity dispersion  $\sigma_0 = 170 \text{ km s}^{-1}$ .

these effects, we chose to extract the sky spectra from the outer most regions of our fully merged science data cube, where no galaxy light was appreciable. The sky was then subtracted optimally as described below.

### 3. ANALYSIS

#### 3.1. Two-dimensional stellar kinematics

To measure reliable stellar kinematics we first co-add spectra using the adaptive spatial two dimensional binning scheme of Cappellari & Copin (2003) to obtain in each resulting (Voronoi) bin a minimum signal-to-noise ratio (S/N). The resulting spectra are spectrally rebinned to steps of constant  $\ln \lambda$ , equivalent to a sampling of  $24 \text{ km s}^{-1}$  per pixel. We adopt the single stellar population (SSP) models of Vazdekis et al. (2003) as spectral templates, which are convolved to have the same effective instrumental broadening as the GMOS data. Next, using an updated version (v4.2) of the penalized pixel-fitting (pPXF) algorithm of Cappellari & Emsellem (2004), a non-negative linear combination of these templates is convolved with a Gaussian line-of-sight velocity distribution (LOSVD) and fit to each observed spectrum, to derive the mean line-of-sight velocity  $V$  and velocity dispersion  $\sigma$  per bin on the plane of the sky. This version

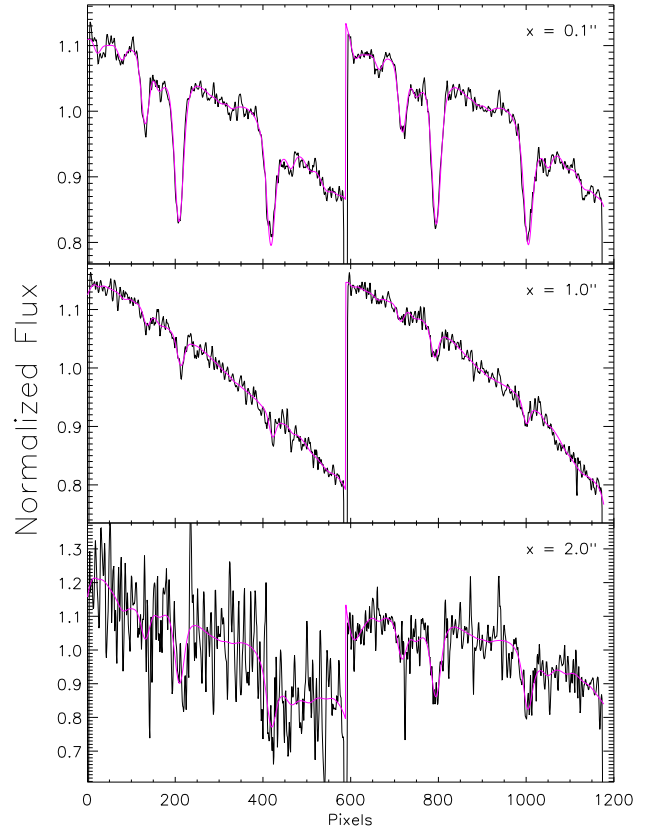


FIG. 3.— Symmetrized fits to (sky-subtracted) spectra at three different positions along the major axis. Each panel shows the two spectra on opposite positions from the center at a distance of  $0.1''$  (top),  $1.0''$  (middle), and  $2.0''$  (bottom). Assuming (axi)symmetry with respect to the minor axis, the same composite stellar population model is fitted to both sides, apart from an opposite sign in the centroid velocity. This symmetrized fitting not only reduces impact of systematic effects in the data, but also increases the effective signal-to-noise. This can significantly improve the extracted kinematics, as can already be seen from the bottom panel where the left spectrum is of lesser quality than the right spectrum, and from the full kinematic maps in Fig. 4. In the middle panel, the contribution (in this case contamination) from the quasar source is clearly visible, and even though the fits to the Ca II triplet still look reasonable the corresponding position is excluded.

of the code allows for the inclusion of a sky spectrum into the set of stellar templates, and determines the optimal scaling of the sky to the overall spectrum (see also Weijmans et al. 2009). We used this procedure to *clean* the individual spectra in our merged data cube, before we derived the final stellar kinematics.

As an example of how this routine performed, we show in the top panel of Fig. 2 the observed spectrum from the center of the lens galaxy (thick black curve), and the cleaned galaxy spectrum (thin black curve) fitted by a composite of stellar population models (blue curve). The sky emission-lines can severely affect the Ca II triplet absorption lines that we use to extract the stellar kinematics, especially at larger radii where the the relative contribution from the sky is more significant. In particular, in our experiments, a poor sky subtraction caused significant systematic effects in the map of  $\sigma$  at the receding side of the galaxy, where one of the absorption lines is redshifted onto (the residual of) a sky emission line.

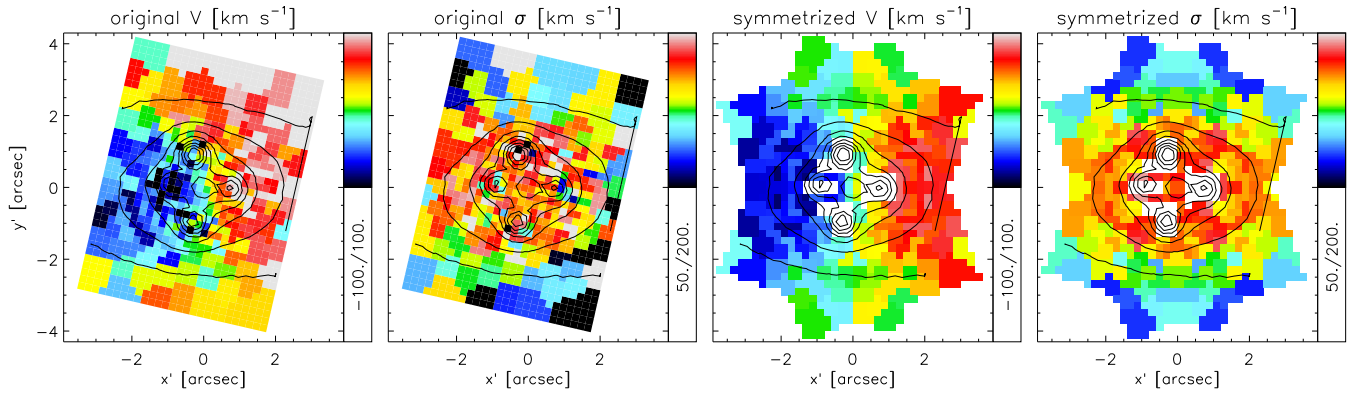


FIG. 4.— Mean line-of-sight velocity  $V$  and velocity dispersion  $\sigma$  maps of the lens galaxy in the Einstein Cross as measured from observations with the integral-field spectrograph GMOS on Gemini-North. At the right side of each map, the (linear) scale in  $\text{km s}^{-1}$  is indicated by the color bar, and the limits are given below. The third and fourth panel show the  $V$  and  $\sigma$  maps after symmetrization assuming oblate axisymmetry (see § 3.1). The overplotted (black) contours show the isophotes of the image reconstruction from collapsing the unsymmetrized data cube, highlighting the regions excluded in the symmetrized kinematics due to contamination from the quasar images. The  $V$  map shows clear and regular rotation around the (vertically aligned) short axis of the bulge. The  $\sigma$  map shows a weak gradient decreasing towards the edge of the field.

The map of  $V$ , however, was (nearly) unaffected, showing regular rotation with a straight zero-velocity curve that coincides with the minor axis of the (bulge) photometry. These tests already show that, at least in the inner parts of the lens galaxy, both the photometry and kinematics are consistent with axisymmetry.

If we now *assume* this symmetry from the start and apply it during the extracting of the stellar kinematics, we can not only increase the S/N, but at the same time also suppress or even remove systematic effects. To do this, we make use of a built-in functionality in the pPXF algorithm that allows diametrically opposed spectra to be fitted simultaneously. The symmetry imposed by this technique can be either mirror-symmetric or point-symmetric, corresponding to the behavior of the LOSVD in axisymmetric or triaxial stellar systems, respectively. In practice, this is done following the method outlined by Rix & White (1992), whereby the two spectra from opposed positions in the galaxy are laid end-to-end to create a single vector. The template library is also doubled in length, where the second half is convolved by the symmetric counterpart of the broadening function used for the first half (simply reflecting the broadening kernel around the systemic velocity). The two galaxy spectra are therefore fitted simultaneously, with the implied assumption of symmetry.

Performing a symmetric extraction of the kinematics presents a number of advantages, and has been used by numerous authors not just as a quality-check (e.g. Rix & White 1992), but also when the assumption of symmetry is an integral part of the analysis (e.g. Gebhardt et al. 2003). The two main advantages for the case presented here are in reducing the impact of systematic effects in the data (including sky subtraction) and increasing the effective spatial resolution. The latter is possible since under the assumption of axisymmetry, all moments of the LOSVD are symmetric about the galaxy major axis. We can therefore ‘fold’ the data cube about the major axis, combining spectra from the two hemispheres, which increases the effective S/N within a given spatial element, and therefore reduces the required spatial bin size.

We interpolate the merged GMOS data cube onto a new spatial grid with  $x'$  and  $y'$  coordinates parallel to the major and minor photometric axes respectively. We then fold the data-cube about the major axis by summing together spatial pixels (‘spaxels’) with equal  $(x, |y|)$  positions. Before spatially binning the spectra to a minimum S/N, the folded data cube is folded again, into a single quadrant by combining spaxels with equal  $(|x|, y)$  positions. The Voronoi bins are derived in this quadrant, and the resulting bin centers are mirrored around  $x' = 0$ . The spectra are combined according to these Voronoi bins to ensure symmetry around the minor axis. At the field perimeter, it is generally not the case that both sides of the galaxy are sampled at the exact same positions, due to the alignment of the GMOS field with respect to the galaxy’s principle axes. This results in some bins where the S/N of the opposed spectra is far from equal, or in some cases where observations are only present on one side of the galaxy. The former is taken into account by consideration of the error spectrum of each bin. For the latter, the bin is fitted as a single spectrum, giving kinematic values only at that position, without a mirrored counterpart. Fig. 3 shows how the (axi)symmetric kinematic extraction performed at three different position along the major axis.

From Monte-Carlo simulations for data of this spectral range and resolution, a minimum S/N of 20 is deemed optimal. This results in an average error in both  $V$  and  $\sigma$  of about  $9 \text{ km s}^{-1}$ , while still preserving the spatial resolution of the data. However, towards the edge of the GMOS field, the errors increase to  $\sim 15 \text{ km s}^{-1}$  in  $V$  and  $\sim 20 \text{ km s}^{-1}$  in  $\sigma$ . The final symmetrically binned data cube consists of  $4 \times 71 = 284$  bins, with the largest containing 19 individual  $0.2''$  spaxels. The resulting (original and symmetrized) maps of  $V$  and  $\sigma$  are presented in Fig. 4, with superposed contours of the integrated flux from the data cube. The velocity map shows regular rotation with amplitude of  $V$  up to  $\sim 100 \text{ km s}^{-1}$ . The dispersion map shows somewhat higher values of  $\sigma$  at the position of the quasar images. This is caused by imperfect subtraction of the quasar continuum, which acts to strongly dilute the absorption lines and make them appear broader.

In our stellar template fit to the observed spectra, we include additive polynomials up to 10th order to account for remaining systematic effects in the data, e.g. due to imperfect flat fielding. At the same time, we use these additive components to mimic the contaminating contribution of the quasar images, which impart a strong featureless continuum on top of the galaxy's integrated stellar spectrum. This method nicely removes nearly all contribution from the quasar, except where the quasar images are the brightest, in which case  $\sigma$  cannot be reliably measured. The middle panel of Fig. 3 provides an example of such a case in which the spectra come from the opposite positions  $1.0''$  from the center along the major axis, right in the middle of two quasar images. Even though the composite stellar population model fits to the Ca II triplet still look reasonable, we exclude these regions when we fit dynamical models to the  $V$  and  $\sigma$  maps. However, between the quasar images, the spectra are dominated by the stellar light of the galaxy, giving a reliable central ( $R < 1''$ ) dispersion  $\sigma_0 \simeq 170 \pm 9 \text{ km s}^{-1}$ . Likewise, at the edges of the field, the quasar contamination is small, providing a reliable gradient in the velocity dispersion.

Comparing in Fig. 4 the symmetrized stellar kinematics with what is obtained without imposing axisymmetry, there is a marked reduction of noise and systematic effects, especially in the velocity dispersion map. However, the main features of regular rotation, decreasing  $\sigma$  at larger radii, as well as corresponding velocity and dispersion amplitudes, are present in both approaches, albeit with larger uncertainty and systematics in the non-symmetrized case. Given the various advantages, we consider hereafter the symmetrically extracted kinematics.

### 3.2. Dynamical models

As mentioned above, both the photometry and (un-symmetrized) kinematics in the inner parts of the lens galaxy are consistent with axisymmetry. Hence, in constructing dynamical models we consider an axisymmetric stellar system in which both the potential  $\Phi(R, z)$  and distribution function (DF) are independent of azimuth  $\phi$  and time. By Jeans' (1915) theorem the DF only depends on the isolating integrals of motion:  $f(E, L_z, I_3)$ , with energy  $E = (v_R^2 + v_\phi^2 + v_z^2)/2 + \Phi(R, z)$ , angular momentum  $L_z = Rv_\phi$  parallel to the symmetry  $z$ -axis, and a third integral  $I_3$  for which in general no explicit expression is known. However, usually<sup>12</sup>  $I_3$  is invariant under the change  $(v_R, v_z) \rightarrow (-v_R, -v_z)$ . This implies that the mean velocity is in the azimuthal direction ( $\overline{v_R} = \overline{v_z} = 0$ ) and the velocity ellipsoid is aligned with the rotation direction ( $\overline{v_R v_\phi} = \overline{v_\phi v_z} = 0$ ).

Schwarzschild (1979) introduced a method that sidesteps our ignorance about the non-classical integrals of motion. It finds the set of weights of orbits computed in an arbitrary gravitational potential that best reproduces all available photometric and kinematic data at the same time. The method has proved to be powerful in building detailed spherical and axisymmetric models of nearby galaxies (e.g. Rix et al. 1997; van der Marel et al. 1998; Gebhardt et al. 2003; Valluri et al. 2004; Cappellari et al. 2006; Thomas et al.

2007) as well as globular clusters (van de Ven et al. 2006; van den Bosch et al. 2006), and since recently also triaxial models (van de Ven et al. 2008; van den Bosch et al. 2008). However, in all cases the stellar systems are significant closer than the lens galaxy in the Einstein Cross, allowing for (even) more and higher-order stellar kinematic measurements necessary to constrain the large freedom in this general modeling method. Instead we construct simpler, but still realistic dynamical models based on the solution of the axisymmetric Jeans equations.

When we multiply the collisionless Boltzmann equation in cylindrical coordinates by respectively  $v_R$  and  $v_z$  and integrate over all velocities, we obtain the two Jeans equations (see also Binney & Tremaine 1987, eq. 4-29)

$$\frac{\partial(R\nu\overline{v_R^2})}{\partial R} + R\frac{\partial(\nu\overline{v_R v_z})}{\partial z} - \nu\overline{v_\phi^2} + R\nu\frac{\partial\Phi}{\partial R} = 0, \quad (1)$$

$$\frac{\partial(R\nu\overline{v_R v_z})}{\partial R} + R\frac{\partial(\nu\overline{v_z^2})}{\partial z} + R\nu\frac{\partial\Phi}{\partial z} = 0, \quad (2)$$

where  $\nu(R, z)$  is the intrinsic luminosity density. Due to the assumed axisymmetry, all terms in the third Jeans equation, that follows from multiplying by  $v_\phi$ , vanish.

We are thus left with four unknown second order velocity moments  $\overline{v_R^2}$ ,  $\overline{v_z^2}$ ,  $\overline{v_\phi^2}$  and  $\overline{v_R v_z}$  and only two equations. This means we have to make assumptions about the velocity anisotropy, or in other words the shape and alignment of the velocity ellipsoid. In case the velocity ellipsoid is aligned with the cylindrical  $(R, \phi, z)$  coordinate system  $\overline{v_R v_z} = 0$ , so that we can readily solve equation (2) for  $\overline{v_z^2}$ . If we next assume a constant flattening of the velocity ellipsoid in the meridional plane, we can write  $\overline{v_R^2} = \overline{v_z^2}/(1 - \beta_z)$  and solve equation (1) for  $\overline{v_\phi^2}$ . This assumption provides in general a good description for the kinematics of real disk galaxies (Cappellari 2008), such as the lens galaxy in the Einstein Cross, which is an early-type spiral galaxy. When  $\beta_z = 0$ , the velocity distribution is isotropic in the meridional plane, corresponding to the well-known case of a two-integral DF  $f(E, L_z)$  (e.g. Lynden-Bell 1962; Hunter 1977).

Knowing the intrinsic second-order velocity moments, the line-of-sight second-order velocity moment for a stellar system viewed at an inclination  $i > 0$  away from the  $z$ -axis follows as

$$\begin{aligned} \overline{v_{\text{los}}^2} = \frac{1}{I(x', y')} \int_{-\infty}^{+\infty} \nu \left[ \left( \overline{v_R^2} \sin^2 \phi + \overline{v_\phi^2} \cos^2 \phi \right) \sin^2 i \right. \\ \left. + \overline{v_z^2} \cos^2 i - \overline{v_R v_z} \sin \phi \sin(2i) \right] dz', \quad (3) \end{aligned}$$

where  $I(x', y')$  is the (observed) surface brightness with the  $x'$ -axis along the projected major axis. For each position  $(x', y')$  on the sky-plane,  $\overline{v_{\text{los}}^2}$  yields a prediction of the second velocity moment  $V^2 + \sigma^2$ , which is a combination of the (observed) mean line-of-sight velocity  $V$  and velocity dispersion  $\sigma$ .

Under the above assumptions, besides the anisotropy parameter  $\beta_z$  (and possibly the inclination  $i$ ), the only unknown quantity is the gravitational potential. In other words, once the gravitational potential is known, the second velocity moment, together with the assumed velocity anisotropy, define which stellar orbits are present, except

<sup>12</sup> If resonances are present,  $I_3$  may lose this symmetry.

for their sense of rotation. Almost any velocity field  $V$  can then be reproduced by arranging the sense of rotation of the individual orbits, without any change to the gravitational potential. The only limit on  $V$  is when all the orbits rotate in the same direction, but this limit is not very useful since it is generally much larger than the observed velocity in galaxies. This implies that, unless further assumptions are made, the observed velocity  $V$  is virtually useless for determining the gravitational potential. Henceforth, we use the combined  $V^2 + \sigma^2$  to constrain the gravitational potential.

The gravitational potential is via Poisson's equation related to the total mass density  $\rho(R, z)$ . We may estimate the latter from the intrinsic luminosity density  $\nu(R, z)$ , derived from deprojecting the observed surface brightness  $I(x', y')$ , once we know the total mass-to-light ratio  $\Upsilon_{\text{tot}}$ . It is common in dynamical studies of the inner parts of galaxies to consider  $\Upsilon_{\text{tot}}$  as an additional parameter and to assume its value to be constant, i.e., mass follows light (e.g. Cappellari et al. 2006). Since  $\Upsilon_{\text{tot}}$  may be larger than the stellar mass-to-light ratio  $\Upsilon_*$ , this still allows for possible dark matter contribution, but with constant fraction. As an alternative to these constant- $\Upsilon_{\text{tot}}$  models, we also construct dynamical models in which we use the strong gravitational lensing to constrain the gravitational potential. In § 3.3 below, we use the positions and relative fluxes of the quasar images to estimate the surface mass density  $\Sigma(x', y')$ , which we deproject to obtain  $\rho(R, z)$ , so that  $\Upsilon_{\text{tot}}$  is not anymore a free parameter. For both type of dynamical models, the best-fits to the stellar kinematic data are shown in Fig. 8, and discussed further in § 4.2 below.

We use the Multi-Gaussian Expansion method (MGE; Monnet et al. 1992; Emsellem et al. 1994) to parameterize both the observed surface brightness  $I(x', y')$  as well as the estimated surface mass density  $\Sigma(x', y')$  as a set of two-dimensional Gaussians. Even though Gaussians do not form a complete set of functions, in general surface density distributions are accurately reproduced, including deviations from an elliptical distribution and ellipticity variations with radius. Representing also the point-spread function (PSF) by a sum of Gaussians, the convolution with the PSF becomes straightforward. Moreover, the MGE-parameterization has the advantage that the deprojection can be performed analytically once the viewing angle(s) are given. Also many intrinsic quantities such as the potential can be calculated by means of simple one-dimensional integrals. Similarly, the calculation of  $\overline{v_{\text{los}}^2}$  in equation (3) reduces from the (numerical) evaluation of in general a triple integral to a straightforward single integral (for further details and a comparison with more general dynamical models see Cappellari 2008). The latter integral is given in Appendix A, together with expressions for  $\nu(R, z)$  and  $\Phi(R, z)$  for the MGE-parameterization of  $I(x', y')$  and  $\Sigma(x', y')$  as given in Table 2, and further discussed in § 4.1 below. We used the publically available Jeans Anisotropic MGE (JAM) implementation<sup>13</sup> to compute  $\overline{v_{\text{los}}^2}$ , also including PSF convolution and sampling over the GMOS lenslets.

### 3.3. Lens models

Under the thin-lens approximation, the gravitational lensing properties of a galaxy are characterized by its potential projected along the line-of-sight, also known as the deflection potential  $\phi(x', y')$ . In case of a MGE parameterization of the surface mass density of the galaxy, the projection along the line-of-sight of the corresponding gravitational potential, or, alternatively, solving the two-dimensional Poisson equation becomes straightforward. The calculation of  $\phi(x', y')$  and its derivatives reduce to the (numerical) evaluation of a single integral, as shown in Appendix A.2 for an axisymmetric system. This MGE approach thus provides a powerful technique to build general lens models. However, since in this case the quasar images only provide a few constraints within a limited radial range, we adopt instead a simpler and less general approach.

We use the algorithm of Evans & Witt (2003) to construct a lens model that accurately fits the (optical) positions and relative (radio) fluxes of the four quasar images in the Einstein Cross. The deflection potential is assumed to be a scale-free function  $\phi(R, \theta) = R^\alpha F(\theta)$  of the polar coordinates  $R$  and  $\theta$  in the lens sky-plane, with  $0 < \alpha < 2$  for realistic models. The angular part  $F(\theta)$  is expanded as a Fourier series

$$F(\theta) = \frac{1}{2} c_0 + \sum_{m=1}^n [c_m \cos(m\theta) + s_m \sin(m\theta)]. \quad (4)$$

The positions  $(x_i, y_i) = (R_i \cos \theta_i, R_i \sin \theta_i)$  of the images are related to the position  $(\xi, \eta)$  of the source by the lens equation (e.g. Schneider et al. 1992)

$$\begin{aligned} \xi &= x_i [1 - (\alpha F_i - \tan \theta_i F'_i) R_i^{\alpha-2}], \\ \eta &= y_i [1 - (\alpha F_i + \cot \theta_i F'_i) R_i^{\alpha-2}], \end{aligned} \quad (5)$$

where  $F_i \equiv F(\theta_i)$  and  $F'_i$  denotes the derivative to  $\theta_i$ . The flux ratios of the images follow from their magnifications  $\mu_i$ , which are given by

$$\begin{aligned} (p_i \mu_i)^{-1} &= 1 - (\alpha^2 F_i + F_i'') R_i^{\alpha-2} \\ &+ (\alpha - 1) \left[ \alpha^2 F_i^2 - (\alpha - 1) F_i'^2 + \alpha F_i F_i'' \right] R_i^{2(\alpha-2)}, \end{aligned} \quad (6)$$

where  $p_i$  is the parity of image  $i$ .

Since the Fourier coefficients  $c_1$  and  $s_1$  correspond to a displacement of the source position  $(\xi, \eta)$ , we set  $c_1 = s_1 = 0$  to remove this degeneracy. For a given slope  $0 < \alpha < 2$ , we are left with  $2n + 1$  free parameters  $(\xi, \eta, c_2, s_2, \dots, c_n, s_n)$  and eleven constraints (four image positions and three flux ratios).

For each image position  $(x_i, y_i)$ , we obtain through the lens equation (5) a prediction of the source position  $(\tilde{\xi}_i, \tilde{\eta}_i)$ , which we compare with the assumed free parameter values  $(\xi, \eta)$  for the source position by evaluating

$$\chi_{\text{src}}^2 = \sum_{i=1}^4 \left[ \frac{(\xi - \tilde{\xi}_i)^2}{\Delta_{xx,i}^2} + 2 \frac{(\xi - \tilde{\xi}_i)(\eta - \tilde{\eta}_i)}{\Delta_{xy,i}^2} + \frac{(\eta - \tilde{\eta}_i)^2}{\Delta_{yy,i}^2} \right], \quad (7)$$

where the weights in the source position are given by

$$\frac{1}{\Delta_{st,i}^2} = \frac{m_{xs,i} m_{xt,i}}{\Delta_{x,i}^2} + \frac{m_{ys,i} m_{yt,i}}{\Delta_{y,i}^2}. \quad (8)$$

The conversion from the uncertainties in the observed

<sup>13</sup> Available from <http://purl.org/cappellari/idl>

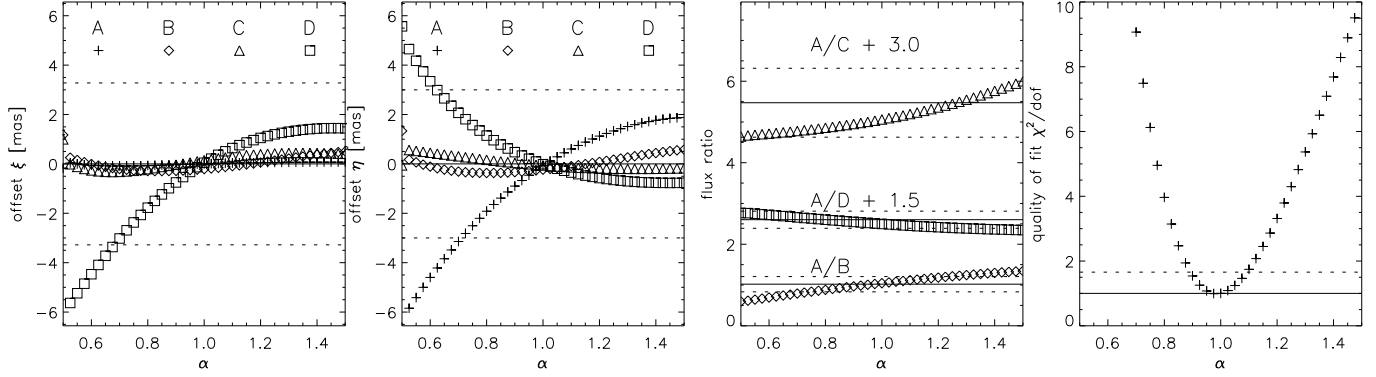


FIG. 5.— Lens model with  $n = 4$  Fourier terms (see § 3.3 for details) fitted to the position of the quasar source (first two panels, in milliarcseconds) and to the observed radio flux ratios of the quasar images (third panel). Over the full range of slopes  $0.5 < \alpha < 1.5$ , the predicted source positions from each quasar image A through D (as indicated by the different symbols) fall within the observed error (dotted lines). However, the recovery of the observed flux ratios (solid lines) within the observed errors (dotted lines) places constraints on the slope. The minimum reduced  $\chi^2$  value of about unity in the fourth panel shows that for  $\alpha \simeq 1.0$  a good overall best-fit model is obtained, with corresponding 99%-confidence interval (dotted line) of  $0.9 \lesssim \alpha \lesssim 1.1$ .

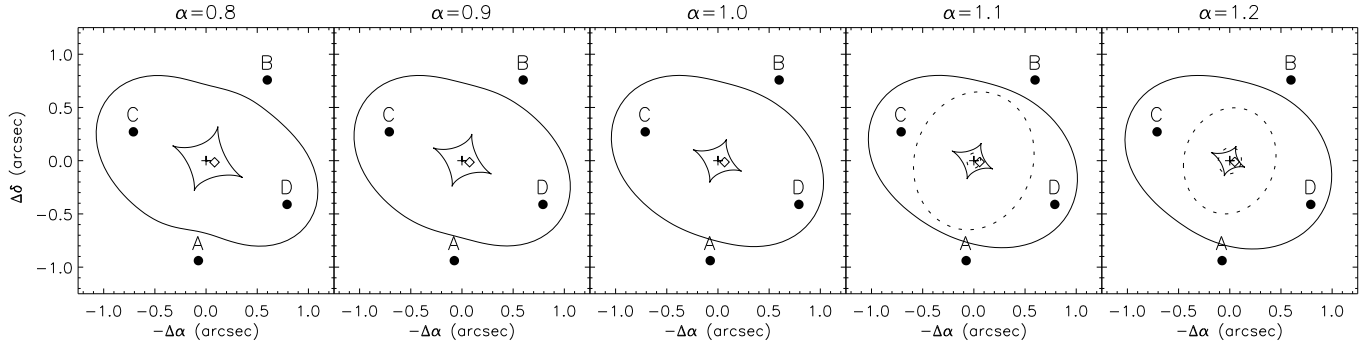


FIG. 6.— Best-fit lens models for five different values of the slope  $\alpha$  indicated at the top of each panel (see Fig. 5 for corresponding quality of the fit). The filled circles indicate the positions of the four quasar images, the cross represents the center of the lens galaxy, and the diamond shows the best-fit position of the quasar source. The smooth and pinched solid curves show respectively the tangential critical curve and radial caustic. The dashed curves are the radial counterparts when they exist (for  $\alpha > 1.0$ ).

TABLE 1  
LENS MODEL PARAMETERS

$\alpha$	$\xi$	$\eta$	$c_0$	$c_2$	$c_3$	$c_4$	$s_2$	$s_3$	$s_4$	$R_E$	$M_E$	$M_c$
0.8	0.0829	-0.0148	2.1615	-0.0588	0.0000	0.0018	0.0589	0.0021	0.0029	0.8858	1.5413	1.5998
0.9	0.0738	-0.0141	1.9457	-0.0493	0.0001	0.0011	0.0499	0.0005	0.0019	0.8862	1.5426	1.5845
1.0	0.0651	-0.0132	1.7733	-0.0415	0.0002	0.0006	0.0423	-0.0007	0.0012	0.8866	1.5441	1.5756
1.1	0.0569	-0.0121	1.6325	-0.0350	0.0004	0.0003	0.0357	-0.0014	0.0008	0.8872	1.5460	1.5708
1.2	0.0490	-0.0110	1.5153	-0.0293	0.0005	0.0001	0.0300	-0.0020	0.0006	0.8878	1.5481	1.5688

NOTE. — Parameters of the lens models shown in Fig. 6. For each slope  $\alpha$ , the best-fit quasar source position  $(\xi, \eta)$  and Fourier coefficients  $c_m$  and  $s_m$  ( $c_1 = s_0 = s_1 = 0$ ) are given, all in arcseconds. The last three columns provide the Einstein radius (in arcsec), the projected mass within this radius and within the critical curve (both in  $10^{10} M_\odot$ ).

image positions  $(\Delta_{x,i}, \Delta_{y,i})$  in the image plane to uncertainties in the source position in the source plane involves the magnification tensor<sup>14</sup> with components

$$\begin{aligned}
 m_{xx,i} &= (p_i \mu_i) (1 - \phi_{yy,i}), \\
 m_{yy,i} &= (p_i \mu_i) (1 - \phi_{xx,i}), \\
 m_{xy,i} &= (p_i \mu_i) \phi_{xy,i}.
 \end{aligned} \tag{9}$$

While the expression for the magnification  $\mu_i$  is given

<sup>14</sup> We implicitly assume here that the deviation between predicted and assumed source position is small enough that the magnification is nearly constant (see also Keeton 2001).

in equation (6), those for the partial derivatives of the deflection potential follow as

$$\begin{aligned}
 \phi_{xx,i} &= \{ [\alpha^2 \cos^2 \theta_i^2 - \alpha(\cos^2 \theta_i^2 - \sin^2 \theta_i^2)] F_i \\
 &\quad - 2(\alpha - 1) \sin \theta_i \cos \theta_i F'_i + \sin^2 \theta_i F''_i \} R_i^{\alpha-2}, \\
 \phi_{yy,i} &= \{ [\alpha^2 \sin^2 \theta_i^2 + \alpha(\cos^2 \theta_i^2 - \sin^2 \theta_i^2)] F_i \\
 &\quad + 2(\alpha - 1) \sin \theta_i \cos \theta_i F'_i + \cos^2 \theta_i F''_i \} R_i^{\alpha-2}, \\
 \phi_{xy,i} &= \{ \alpha(\alpha - 2) \sin \theta_i \cos \theta_i F_i - \sin \theta_i \cos \theta_i F''_i \\
 &\quad + (\alpha - 1)(\cos^2 \theta_i^2 - \sin^2 \theta_i^2) F'_i \} R_i^{\alpha-2}.
 \end{aligned} \tag{10}$$

Next, we turn the predicted magnifications  $\tilde{\mu}_i$  through equation (6) per image into predictions for the flux ratios  $\tilde{f}_j \equiv \tilde{\mu}_1/\tilde{\mu}_{1+j}$ . We compare them to the observed flux ratios  $f_j$  with corresponding errors  $\Delta f_j$  by evaluating

$$\chi_{\text{fix}}^2 = \sum_{j=1}^3 \frac{(f_j - \tilde{f}_j)^2}{\Delta f_j^2}. \quad (11)$$

We can now find the best-fit parameters by minimizing

$$\chi^2 = \chi_{\text{src}}^2 + \chi_{\text{fix}}^2 + \lambda \sum_{m \geq 3}^n (c_m^2 + s_m^2), \quad (12)$$

with  $\lambda \geq 0$  a constant. The last term guides the solution towards a smooth, realistic lens model by penalizing (strong) deviations from an elliptic shape.

For a range of slopes  $0.5 < \alpha < 1.5$ , the fits of the above lens model with  $n = 4$  Fourier terms are shown in Fig. 5. Whereas the predictions of the source position remain within the observed errors over the full range of slopes, the recovery of the observed radio fluxes places constraints on the slope. Dividing the corresponding  $\chi^2$  values by the ten degrees of freedom (eleven constraints minus the slope parameter) provides a quality of fit, shown in the lower-right panel of Fig. 5. The minimum value  $\chi^2/10 \simeq 1$  shows that for  $\alpha \simeq 1.0$  a good overall best-fit model is obtained. The corresponding 99%-confidence interval (dotted line) is  $0.9 \lesssim \alpha \lesssim 1.1$ .

With  $n < 4$  Fourier terms the fits are significantly worse ( $\chi^2/10 > 2.5$ ), and with  $n = 5$  Fourier terms the fit does not improve (for  $n > 5$  the fitting problem becomes underdetermined). If we replace the radio fluxes by the optical fluxes from the CASTLES website, no acceptable lens model fit is possible ( $\chi^2/10 > 30$ ). On the other hand, the mid-infrared fluxes from Agol et al. (2000) yield similar good fits as the radio fluxes. The best-fit slope  $\alpha = 0.9$  is lower because the fluxes of image A and C are respectively about 10% and 30% lower than in the radio. Image C is the faintest in both mid-infrared and radio, while image D is the faintest in the optical. Since the radio is expected to be (much) less affected by differential extinction and microlensing, we adopt the corresponding lens models.

In the investigation below, we use the lens models with slopes  $\alpha = \{0.8, 0.9, 1.0, 1.1, 1.2\}$ , shown in Fig. 6, and with best-fit parameters given in Table 1. The critical curves  $R_c(\theta)$  are obtained by solving the (quadratic) equation (6) for infinite magnification, i.e., for vanishing left-hand-side. The caustics then follow upon substitution of  $R_c(\theta)$  in the lens equation (5). We see in Fig. 6 that even the two models outside the 99%-confidence interval for  $\alpha$  are relatively smooth as expected for a realistic galaxy model.

The surface mass density of the lens models follows from Poisson's equation as

$$\Sigma(R, \theta) = \Sigma_c \frac{1}{2} [\alpha^2 F(\theta) + F''(\theta)] R^{\alpha-2}, \quad (13)$$

with the critical surface mass density defined as

$$\Sigma_c = \frac{c^2 D_s}{4\pi G D_l D_{ls}}, \quad (14)$$

where  $c$  is the speed of light and  $D_l$ ,  $D_s$  and  $D_{ls}$  are the

TABLE 2  
MULTI-GAUSSIAN EXPANSION PARAMETERS

$i$	$I$ -band surface brightness			$\alpha = 1.0$ lens model		
	$\log I_0$	$\log \sigma'$	$q'$	$\log \Sigma_0$	$\log \sigma'$	$q'$
1	4.329	-1.564	0.700	5.114	-1.398	0.645
2	3.935	-0.942	0.700	4.556	-1.037	0.660
3	3.606	-0.627	0.700	4.238	-0.779	0.662
4	3.293	-0.239	0.700	3.928	-0.544	0.678
5	3.005	-0.043	0.700	3.628	-0.350	0.673
6	2.845	0.230	0.700	3.459	-0.186	0.675
7	2.261	0.587	0.700	3.354	-0.001	0.675
8	2.160	0.917	0.414	3.208	0.220	0.675
9	1.334	1.135	0.700	3.069	0.496	0.675
10	-	-	-	2.991	1.000	0.675

NOTE. — The parameters of the Gaussians in the MGE fit to the HST/WFPC2/F814W  $I$ -band image of the surface brightness (columns 2–4, “deconvolved” with the WFPC2 PSF), and to the surface mass density of the overall best-fit lens model with slope  $\alpha = 1.0$  (columns 5–7) of the lens galaxy in the Einstein Cross (see also Fig. 1). Columns two and five give for each Gaussian component respectively the central surface mass density (in  $M_\odot \text{pc}^{-2}$ ) and the central surface brightness (in  $L_\odot \text{pc}^{-2}$ ), columns three and six the dispersion (in arcsec) along the major axis, and columns four and seven the observed flattening.

(angular diameter) distance to the lens galaxy, the quasar source and the distance from lens to source, respectively.

The (projected) mass within the critical curve

$$M_c = \Sigma_c \int_0^{2\pi} \frac{1}{2\alpha} [\alpha^2 F(\theta) + F''(\theta)] R_c(\theta)^\alpha d\theta, \quad (15)$$

is in general close to the projected mass within the Einstein radius. The latter is the radius  $R_E$  for which the projected mass is equal to the Einstein mass defined as  $M_E = \Sigma_c \pi R_E^2$ . Because  $R_E$  is independent of  $\theta$ , all higher order Fourier terms average out, and we are left with  $R_E^{2-\alpha} = \alpha c_0/2$ , so that the Einstein mass becomes

$$M_E = \Sigma_c \pi \left( \frac{\alpha c_0}{2} \right)^{2/(2-\alpha)}, \quad (16)$$

Since we express all (projected) coordinates on the plane of the sky in arcseconds, including the radius  $R$ , we multiply expressions (15) and (16) by  $(D_l \pi/0.648)^2$  to convert from arcseconds to pc for a given (angular diameter) distance  $D_l$  to the lens galaxy in Mpc.

From the last two columns in Table 1, we see indeed that  $M_c \approx M_E = 1.54 \times 10^{10} M_\odot$ , nearly independent of the slope  $\alpha$ . Taking into account an inverse scaling with the Hubble constant of  $H_0 = 73 \text{ km s}^{-1} \text{ Mpc}^{-1}$ , our values are within a few per cent of previous measurements (e.g. Rix et al. 1992; Wambsganss & Paczynski 1994; Chae et al. 1998; Schmidt et al. 1998; Trott & Webster 2002).

## 4. RESULTS

### 4.1. Luminous versus total mass distribution

In the left and middle panel of Fig. 1 we show MGE fits (contours) to respectively the  $V$ -band and the  $I$ -band HST image, obtained with the software of Cappellari (2002), while masking the quasar images. For each fit we assume the same position angle (PA) for the Gaussians, consistent with the adopted axisymmetry in the dynamical models. Although the bar and spirals cannot be reproduced, it provides a good description of the

disk in the outer parts (left panel) and reproduces well the bulge in the inner parts (middle panel). Similarly, we derive MGE fits to the surface mass density in equation (13) of the best-fit lens models with slopes  $\alpha$  from 0.8 to 1.2. In the right panel of Fig. 1, we show the MGE fit (solid contours) to the surface mass density (dashed contours) of the overall best-fit lens model with slope  $\alpha = 1.0$ . The corresponding parameters are given in Table 2 (columns 5–7), together with the parameters of the MGE fit to the *I*-band surface brightness (columns 2–4). The latter parameters are “deconvolved” using a MGE model fitted to the WFPC2 PSF as determined with Tiny Tim (Krist & Hook 2004).

The Gaussians in the MGE fit to the *I*-band surface brightness have a PA of  $\sim 70^\circ$ , which is similar to the PA of  $\simeq 67^\circ$  in the MGE fit to the surface mass density of lens models. Both these values are consistent with the measurements by Yee (1988), who found a PA of  $\simeq 67^\circ$  for the axis through quasar images C and D, bracketed by a PA of  $\simeq 77^\circ$  for the outer disk and a PA of  $\simeq 39^\circ$  for the bar (see also Fig. 1 of Trott & Webster 2002).

As shown in Fig. 7, not only the orientation, but also the shape of the luminous density distribution as inferred from the surface brightness, is very similar to that of the total mass density distribution as derived from the lens models. The left and middle panel in the top row show respectively the profile and the projected ellipticity  $\epsilon = 1 - q'$  of the surface mass density as function of the major axis on the sky-plane. The thin curves are for the lens models with fixed slope  $\alpha$  (as indicated in the bottom-right panel). The thick solid curve is for the *I*-band surface brightness, multiplied with a constant mass-to-light ratio  $\Upsilon_E = 3.4 \Upsilon_{\odot,I}$ . The latter is derived from dividing the projected mass from the lens models (shown in the top-right panel of Fig. 7) within the Einstein radius, i.e., the Einstein mass  $M_E$ , by the projected luminosity within the Einstein radius  $R_E$ .

We see that around  $R_E$  (indicated by the dashed vertical line), where the lens models are best constrained by the observed quasar image positions and relative flux ratios, both the slope and the ellipticity of the *projected* luminous and total mass density are nearly the same. The same holds true for the corresponding *intrinsic* mass densities, of which the profiles and ellipticities  $\epsilon_{\text{intr}} = 1 - q$  are shown in the left and middle panel in the bottom row of Fig. 7. These (analytic) deprojections (see Appendix A) are under the assumption of oblate axisymmetry and for a given inclination which we derive from the flattening of the disk in the outer parts. We find from the MGE fit to the *V*-band surface brightness (left panel of Fig. 1), that Gaussian components with a measured flattening as small as  $q' \simeq 0.4$  are required for an acceptable fit. This sets a lower limit to the inclination of  $i \gtrsim 66^\circ$  (significantly larger than  $i \simeq 60^\circ$  found by Irwin et al. 1989). Adopting a lower limit for the *intrinsic* flattening of the disk of  $q = 0.15$  (e.g. Lambas et al. 1992), we then obtain an inclination of  $i \simeq 68^\circ$ .

Around  $R_E$  the luminosity density is close to isothermal ( $\rho \propto R^{-2}$  intrinsic or  $\Sigma \propto R^{-1}$  in projection) like the mass density of the overall best-fit lens model. Towards the center the slope of the luminosity density becomes shallower. The (fixed) slope of the lens model is not anymore (well) constrained by the quasar images towards the center, neither for radii a few times  $R_E$ .

At these larger radii also the luminosity density is not only due to the bulge, but the bar and disk start contributing, as can also be seen from the increase in the ellipticity. Nevertheless, within a radius  $R \lesssim 4''$ , the intrinsic luminous and total mass distribution are very similar, i.e., mass follows light. This means we can infer the gravitational potential either from the observed surface brightness adopting a (constant) total mass-to-light ratio  $\Upsilon_{\text{tot}}$ , or directly from the best-fit lens model (see also Appendix A). The corresponding circular velocity curves, defined as  $v_{\text{circ}}^2 = R\partial\Phi/\partial R$  in the equatorial plane, are shown in the bottom-right panel of Fig. 7, using  $\Upsilon_E = 3.4 \Upsilon_{\odot,I}$  as above.

#### 4.2. Axisymmetric Jeans models

In Fig. 8, the second panel in the bottom row shows the square root of the combination  $V^2 + \sigma^2$  of the observed (and symmetrized) mean line-of-sight velocity  $V$  and dispersion  $\sigma$  maps of the lens galaxy (Fig. 4, two panels on the right). The other panels in Fig. 8 show the line-of-sight second-order velocity moment as predicted by the JAM models (Cappellari 2008), which are based on the solution of the axisymmetric Jeans equations as summarized in Appendix A. With a central velocity dispersion of  $\sigma_0 \simeq 170 \text{ km s}^{-1}$ , the  $M_{\text{BH}} - \sigma$  relation as given by Tremaine et al. (2002) predicts a central black hole of mass  $M_{\text{BH}} \simeq 7.0 \times 10^7 M_\odot$  for the lens galaxy. Since the corresponding sphere-of-influence  $M_{\text{BH}}/\sigma^2 \simeq 0.01''$  is not resolved by our kinematic data, we cannot fit for it, but do include the predicted BH in the Jeans models (as an additional Gaussian). Finally, we convolve the predicted second-order velocity moment with the Gaussian PSF of the kinematic data with FWHM =  $1''$ . The (linear) scale in  $\text{km s}^{-1}$ , as indicated by the color bar and limits at the top of the panel with the observations, is the same in all panels of Fig. 8.

The axisymmetric Jeans models in the top row use the gravitational potential inferred from the *I*-band surface brightness, assuming that mass follows light. The corresponding (constant) dynamical mass-to-light ratio  $\Upsilon_{\text{dyn}}$  that provides the best-fit to the observations is indicated at the top, together with the assumed value for the anisotropy parameter  $\beta_Z$ , increasing from left to right. The corresponding increase in the (constant) flattening of the velocity ellipsoid in the meridional plane (or decrease in  $\overline{v_z^2}/\overline{v_R^2}$ ), has two main effects: a less pinched “butterfly” shape and a weaker gradient parallel to the (vertically aligned) short axis. Comparing with the observations, we see that at lower  $\beta_Z$  values the pinching is too strong, while at higher  $\beta_Z$  the gradient along the short axis is too shallow. Therefore, it is not unexpected that the “best-fit” is when  $\beta_Z \simeq 0$  and  $\Upsilon_{\text{dyn}} \simeq 4.0 \Upsilon_{\odot,I}$  (in the *I*-band), but with reduced  $\chi^2 \simeq 3$  significantly above unity.

Part of the latter mismatch might be due to (systematic) discrepancies in the data, in particular due to the challenging measurement of the velocity dispersion. The average uncertainty in the observed second-order velocity moment is about  $10 \text{ km s}^{-1}$ , which translates into an error of around 12 per cent in  $\Upsilon_{\text{dyn}}$ , or about  $0.5 \Upsilon_{\odot,I}$ . However, the uncertainties in the observed second-order velocity moment vary quite a lot, from only  $\sim 2 \text{ km s}^{-1}$  in the center to  $\sim 20 \text{ km s}^{-1}$  at the edge of the GMOS

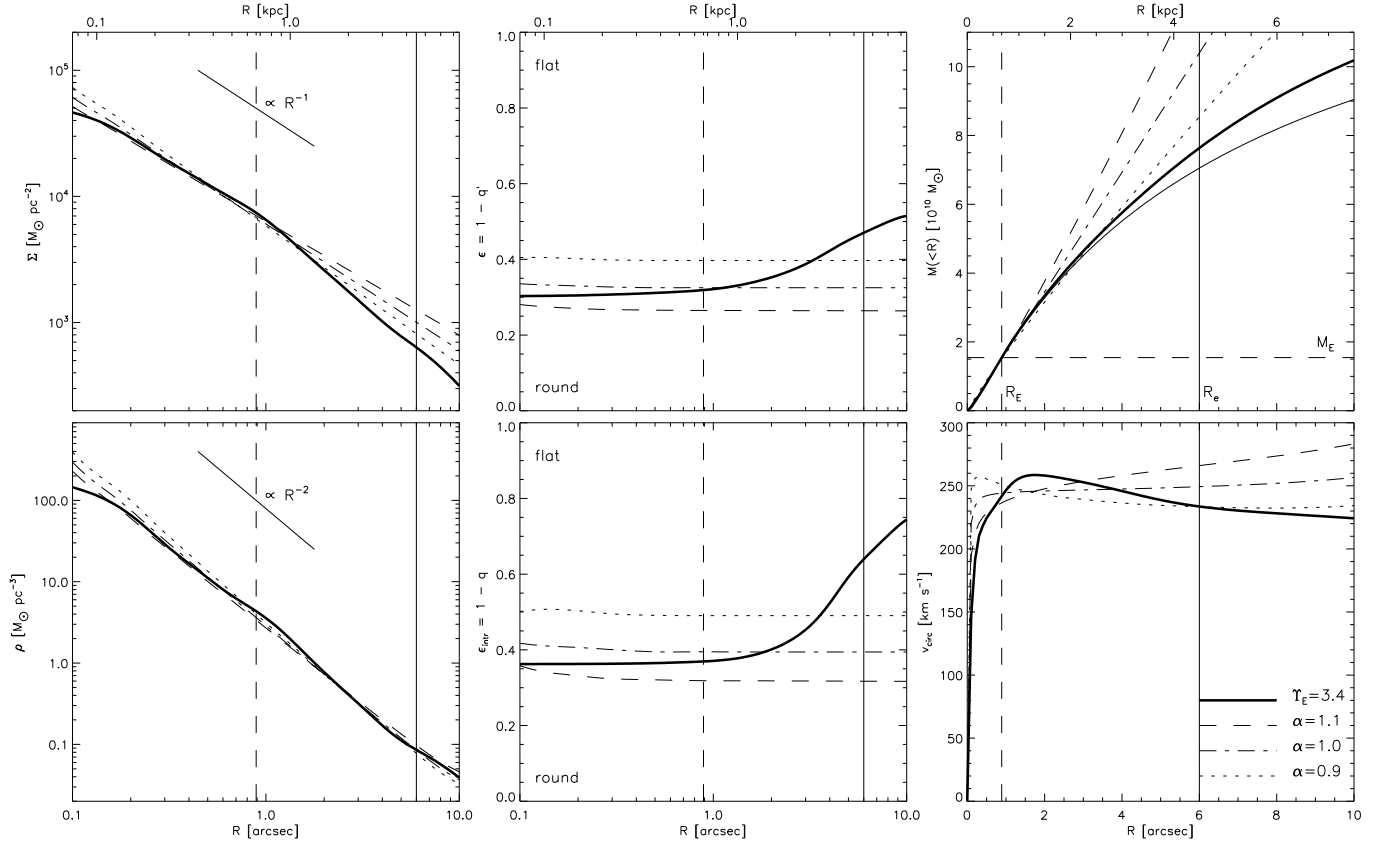


FIG. 7.— Radial profiles of the mass distribution of the lens galaxy in the Einstein Cross as function of radius  $R$ , in arcsec at the bottom and in kpc at the top. In each panel the dashed and solid vertical lines indicate respectively the Einstein radius  $R_E = 0.89''$  and the effective radius  $R_e = 6''$ . The *top panels* shows from left to right the surface mass density profile  $\Sigma$ , the corresponding projected ellipticity  $\epsilon = 1 - q'$ , and the mass  $M$  enclosed within the projected radius  $R$  along the major-axis on the plane of the sky. The dotted, dash-dotted and dashed curves are from the best-fit lens models with (fixed) slopes  $\alpha$  of respectively 0.9, 1.0 and 1.1 (see § 3.3). The thick solid curves are from the observed ( $I$ -band) surface brightness, multiplied with a constant mass-to-light ratio  $\Upsilon_E = 3.4 \Upsilon_{\odot, I}$ . The latter is obtained from dividing the Einstein mass (indicated by the horizontal dashed line in the top-right panel) by the (projected) luminosity within the Einstein radius. The thin solid curve in the top-right panel shows the enclosed projected mass of a de Vaucouleurs profile fitted to the bulge which is dominating the mass in the inner parts of the lens galaxy. The *bottom panels* shows from left to right the mass density profile  $\rho$ , the corresponding intrinsic ellipticity  $\epsilon_{\text{intr}} = 1 - q$ , and the circular velocity  $v_{\text{circ}}$  as function of the radius  $R$  in the meridional plane. These intrinsic quantities are obtained from the MGE fits to the projected density, under the assumption of oblate axisymmetry and for an inclination  $i = 68^\circ$  (see also Appendix A).

field. And although we were very careful in disentangling the contribution from the quasar and excluded the regions at the quasar images, the measured velocity dispersion around these regions might still be systematically affected by (broadening due to) residual light from the quasar source. This possibly explains the observed excess in the observed second-order velocity moment around the quasar images with respect to the accurately measured central value. At the same time, such an excess might mimic a steeper gradient in the observed second-order velocity moment. Indeed, in all Jeans models in the top row of Fig. 8 the prediction at the center is significantly higher than the observed value. As a result, we expect that the dynamical mass-to-light ratio is overestimated.

If, alternatively, we infer the gravitational potential directly, i.e., without the need for a mass-to-light ratio, from the (deprojected) surface mass density of the best-fit lens models, the axisymmetric Jeans models predict maps of the second-order velocity moments that are similar in shape but with lower values near the center. This is shown in the middle row of Fig. 8 for the overall best-fit lens model with slope  $\alpha = 1$ , and for the same range

in anisotropy parameters  $\beta_z$ . The formal best-fit is obtained for  $\beta_z \simeq 0$ , but the observed central value is more closely matched in case of mild velocity anisotropy in the meridional plane with  $\beta_z \gtrsim 0.1$ . For  $\alpha = 0.9$ , i.e., density slopes steeper than isothermal, the observed central value is best matched when  $\beta_z \simeq 0$ , with at the same time a steeper gradient along the short-axis, as shown in the first panel in the bottom row of Fig. 8. The last two panels show that for  $\alpha > 1$ , velocity isotropy in the meridional plane ( $\beta_z = 0$ ) results in a central value much lower than the observed second-order velocity moment.

We conclude that for the lens models with slopes  $\alpha = 1.0 \pm 0.1$ , as constrained by the lensing geometry, and for a mild anisotropic velocity distribution in the meridional plane with  $\beta_z = 0.1 \pm 0.1$ , the predictions of the second-order velocity moments match the accurately measured central value, and follow the gradient within the observational uncertainties outside the region that might be affected by (residual) quasar light. The latter results in broadening of the velocity dispersion, so that the best-fit dynamical mass-to-light ratios we derive when we infer the gravitational potential from the surface

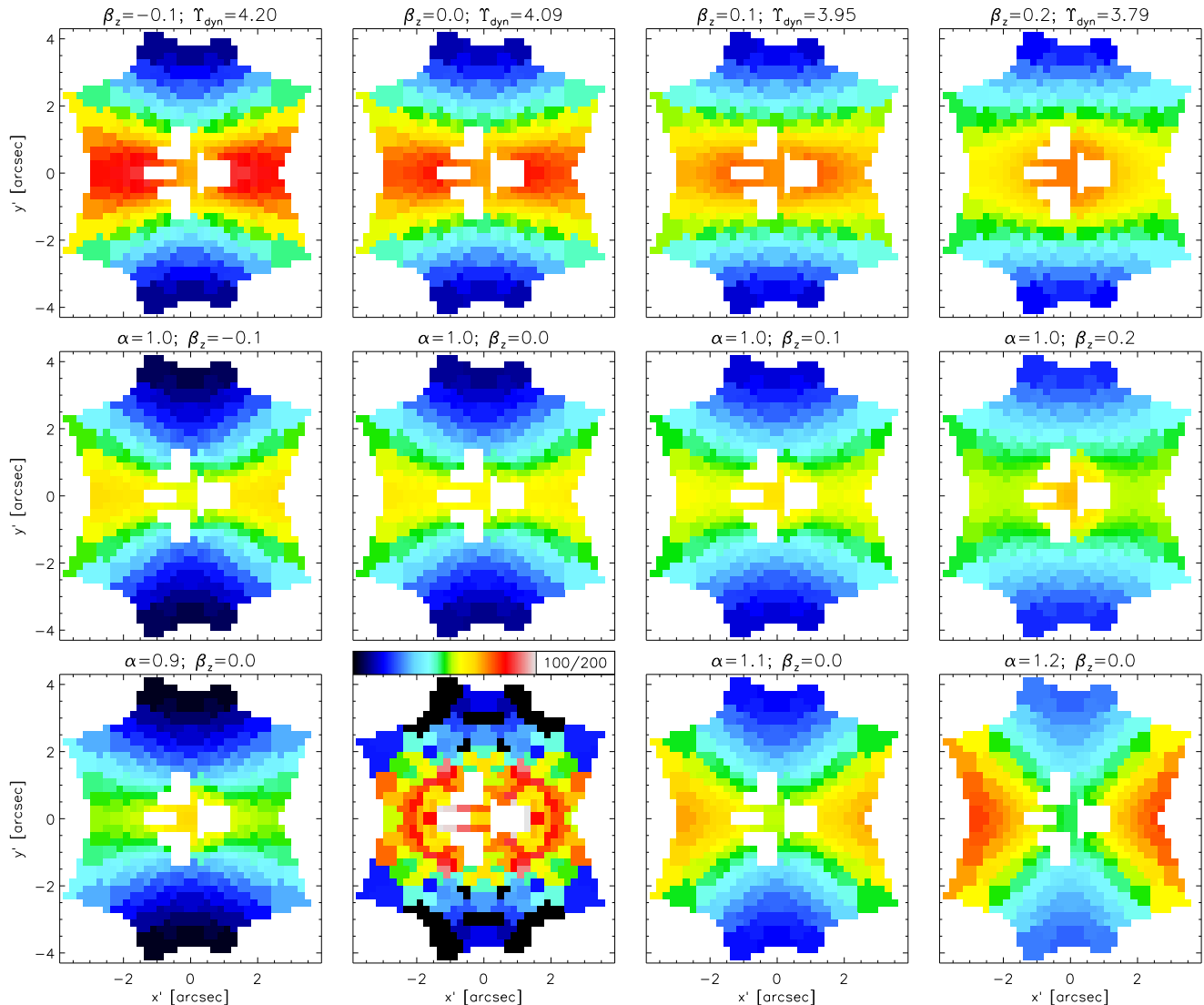


FIG. 8.— Axisymmetric Jeans model of the lens galaxy in the Einstein Cross. The second panel in the bottom row shows the square root of the combination  $V^2 + \sigma^2$  of the observed mean line-of-sight velocity  $V$  and dispersion  $\sigma$  maps (Fig. 4). The (linear) scale in  $\text{km s}^{-1}$  is indicated by the color bar and limits at the top, and is the same for all other panels, which show the line-of-sight second-order velocity moment as predicted by the axisymmetric Jeans models (§ 3.2 and Appendix A.3). In the *top row*, the gravitational potential is inferred from the *I*-band surface brightness, assuming that mass follows light. The corresponding (constant) dynamical mass-to-light ratio  $\Upsilon_{\text{dyn}}$  that provides the best-fit to the observations is indicated at the top, together with the assumed value for the anisotropy parameter,  $\beta_z = 1 - \overline{v_z^2}/\overline{v_R^2}$ , increasing from left to right. The latter parameter represents the (constant) flattening of the velocity ellipsoid in the meridional plane. The *middle row* follows the same sequence of increasing  $\beta_z$  values, but the gravitational potential is now computed directly, i.e., without mass-to-light ratio conversion, from the overall best-fit lens model with slope  $\alpha = 1.0$ . In the *bottom row*, besides the observations in the second panel, the predictions for different slopes  $\alpha$  are shown, with  $\beta_z = 0$ , corresponding to an isotropic velocity distribution in the meridional plane.

brightness, are likely overestimated. Fitting instead only the unaffected and accurately measured second-order velocity moment in the center, we find for  $\beta_z = 0.1$  a best-fit value of  $\Upsilon_{\text{dyn}} \simeq 3.7 \Upsilon_{\odot, I}$ , with an error around  $0.5 \Upsilon_{\odot, I}$ . On the other hand, both the Einstein mass and luminosity within the Einstein radius are well constrained, resulting in at most a few per cent error in  $\Upsilon_E = 3.4 \Upsilon_{\odot, I}$ . Therefore, in what follows, we adopt the latter as the total mass-to-light ratio in the inner bulge-dominated region of the lens galaxy.

In the above axisymmetric Jeans models we fix the inclination to  $i = 68^\circ$  determined from the observed ellipticity of the outer disk (see § 4.1). When we vary the

inclination over a reasonable range above the lower limit  $i \gtrsim 66^\circ$ , there is no significant change in the above results, which is expected because the inclination only has a weak effect on the mass-to-light ratio (see also Fig. 4 of Cappellari et al. 2006).

#### 4.3. Stellar mass-to-light ratio

We have shown that in the bulge-dominated inner region of the lens galaxy, the total mass distribution closely follows the light distribution. This does not mean there is no dark matter present, since if dark matter follows (nearly) the same distribution it might contribute to part of the above estimated total mass-to-light ratio  $\Upsilon_{\text{tot}} \simeq$

$3.4 \Upsilon_{\odot,I}$ . To determine this possible *constant* dark matter fraction, we need to measure the stellar mass-to-light ratio  $\Upsilon_*$ . To this end we use the single stellar population (SSP) models of Vazdekis et al. (1996), adopting as initial reference the Kroupa (2001) initial mass function (IMF) with lower mass cut-off  $0.01 M_{\odot}$  (faintest star  $0.09 M_{\odot}$ ) and upper mass cut-off of  $120 M_{\odot}$ .

We derive a high-S/N spectrum from our data cube by collapsing the central spectra that are unaffected by the quasar images. Even so, the Ca II triplet is equally well fitted by SSP models of nearly all ages and metallicities of about  $[\text{Fe}/\text{H}] = \pm 0.2$  around solar, which leaves the stellar mass-to-light ratio nearly unconstrained. Therefore, we also derived colors from archive HST images (PI: Kochanek). After matching all images, using both the quasar positions and isophotes of the lens galaxy, we compute the magnitudes in a circular aperture of radius  $R = 0.2''$  (well within the quasar images at  $R \simeq 0.9''$ ). After correcting for a Galactic extinction of  $E(B - V) = 0.071$  (Schlegel et al. 1998), we derive in the F555W, F675W, F814W (WFPC2), F160W and F205W (NICMOS2) filters magnitudes of 16.83, 16.03, 15.53, 13.80, and 13.51, respectively. We convert the latter to *rest frame* magnitudes of 16.72, 16.13, 15.50, 13.70, 13.59 in Johnson *V*, *R*, *I*, *H* and *K* filters, respectively. Instead of the standard K-correction, we use the method described in § 3 of van de Ven et al. (2003) to take simultaneously into account the filter responses and the redshift of the lens galaxy.

The resulting colors are best fitted by a SSP model with age  $t \simeq 8$  Gyr and metallicity  $[\text{Fe}/\text{H}] \simeq 0.2$ , corresponding to an *I*-band stellar mass-to-light ratio  $\Upsilon_* \simeq 3.3 \Upsilon_{\odot,I}$ . The  $1\sigma$  confidence limits yield a range in  $t$  from 7 to 14 Gyr, and in  $[\text{Fe}/\text{H}]$  from 0.0 to 0.3, corresponding to a range in  $\Upsilon_*$  from 2.8 to  $4.1 \Upsilon_{\odot,I}$ . The lower limit implies at most  $\sim 20$  per cent of dark matter within  $R \lesssim 4''$ , but the results are fully consistent with no dark matter at all. The SSP models of Maraston (1998, 2005) with a Kroupa IMF yield similar results. Adopting a Salpeter (1955) IMF with the same lower and upper mass cut-offs, increases  $\Upsilon_*$  by about 30 per cent. This not only implies no dark matter, but even for the lower limit  $\Upsilon_* > \Upsilon_{\text{tot}}$ , which is unphysical. This is consistent with evidences for both late-type galaxies (Bell & de Jong 2001) and early-type galaxies (Cappellari et al. 2006) that, if the IMF is universal, a Salpeter IMF is excluded, whereas a Kroupa IMF matches the observations (see de Jong & Bell 2007, for a review).

## 5. DISCUSSION AND CONCLUSIONS

We used the GMOS-North integral-field spectrograph to obtain two-dimensional stellar kinematics of the lens galaxy in the Einstein Cross. In addition to the four bright quasar images and the distance of the lens galaxy ( $D_l = 155$  Mpc), in particular the presence of sky lines in the observed Ca II triplet region made the extraction of the absorption line kinematics challenging. Even so, we were able to derive high-quality line-of-sight velocity  $V$  and dispersion  $\sigma$  maps of the bulge-dominated inner region  $R \lesssim 4''$ , reaching about two-thirds of the effective radius  $R_e \simeq 6''$  of this early-type spiral galaxy. The  $V$  map shows regular rotation up to  $\sim 100 \text{ km s}^{-1}$  around the minor axis of the bulge, consistent with axisymmetry. The  $\sigma$  map shows a weak gradient increasing towards a

central ( $R < 1''$ ) value of  $170 \pm 9 \text{ km s}^{-1}$ .

The only other direct (single) measurement of the velocity dispersion is  $215 \pm 30 \text{ km s}^{-1}$  by Foltz et al. (1992). Adopting their central aperture of  $0.7'' \times 0.4''$  at a position angle of  $39^\circ$  (along the bar), our extracted spectrum is shown in Fig. 2. The lower panel shows sky-subtracted galaxy spectrum (black curve) and our best-fit composite stellar population model (blue curve), yielding a velocity dispersion in this aperture of  $172 \text{ km s}^{-1}$ . The other model (red curve) has the velocity dispersion fixed to  $215 \text{ km s}^{-1}$  as measured by Foltz et al. (1992). Since the observing conditions were similar with seeing around  $0.5''$ , we can directly compare both measurements. We see from residuals at the bottom and the quoted reduced  $\chi^2$ -values that  $172 \text{ km s}^{-1}$  provides a better fit than  $215 \text{ km s}^{-1}$ , particularly in fitting the strongest of the three absorption lines.

In addition, for a singular isothermal sphere lens model, we can use the relation  $\Delta\theta = 8\pi(\sigma_{\text{SIS}}/c)^2 D_{ls}/D_s$  (e.g. Kochanek et al. 2000) with a separation  $\Delta\theta = 1.8''$  of the four quasar images, to obtain a simple estimate for the dispersion of  $\sigma_{\text{SIS}} \simeq 180 \text{ km s}^{-1}$ . Adopting a spherical Jeans model with a range in velocity anisotropy, van de Ven et al. (2003) convert this to a central velocity dispersion of  $168 \pm 17 \text{ km s}^{-1}$  within a circular ‘‘Coma’’ aperture (with a diameter of  $3.4''$  at the distance of the Coma cluster). At the (angular diameter) distance  $D_l = 155$  Mpc of the lens galaxy, this corresponds to a circular aperture with radius of  $1''$ , so that it can be compared directly to our central value of  $170 \pm 9 \text{ km s}^{-1}$ . Finally, King and de Vaucouleurs models of Kent & Falco (1988) predict a similar value of  $\sim 166 \text{ km s}^{-1}$ , and also Barnes et al. (1999) find a value of  $165 \pm 23 \text{ km s}^{-1}$  based on their two H I rotation curve measurements. Hence, it is likely that the long-slit measurement by Foltz et al. (1992) is affected by the bright quasar images, whereas our spatially resolved measurements allow for a clean(er) separation of the quasar contribution.

A large variety of different lens models have been constructed for the Einstein Cross, most of which fit the positions of the quasar images but not their relative flux ratios. Adopting the scale-free lens model of Evans & Witt (2003), we found that fitting at the same time also the (radio) flux ratios constrained the slope of the total mass surface density  $\Sigma \propto R^{\alpha-2}$  to be  $\alpha = 1.0 \pm 0.1$ . The total mass within the Einstein radius  $R_E = 0.89''$ , i.e., the Einstein mass, is  $M_E = 1.54 \times 10^{10} M_{\odot}$ , nearly independent of the slope  $\alpha$ , and consistent with previous measurements in the literature. Dividing by the projected luminosity within  $R_E$ , as measured from the observed *I*-band surface brightness, we obtained a mass-to-light ratio of  $\Upsilon_E = 3.4 \Upsilon_{\odot,I}$ , with an error of at most a few per cent.

We determined the mass-to-light ratio in an additional, independent way by fitting dynamical models to the (combined) observed  $V$  and  $\sigma$  maps. We used the solution of the axisymmetric Jeans equations to predict this second-order velocity moment, with the gravitational potential inferred from the deprojected *I*-band surface brightness, assuming that mass follows light. We expect the resulting best-fit constant mass-to-light ratio to be an overestimation due to possible residual contribution from the quasar light. Even so, restricting the fit to

the unaffected and accurately measured central second-order velocity moment, we found  $\Upsilon_{\text{dyn}} = 3.7 \pm 0.5 \Upsilon_{\odot,I}$ . When we used instead the gravitational potential that follows directly, i.e., without mass-to-light ratio conversion, from the surface mass density of the best-fit lens models, we arrived at a similar prediction of the second-order velocity moment. We showed that the reason is that the luminous and total mass distribution, as inferred from respectively the surface brightness and lens model, are very similar. This implies that the inner region of the lens galaxy mass (closely) follows light, with a total mass-to-light ratio  $\Upsilon_{\text{tot}} \simeq 3.4 \Upsilon_{\odot,I}$ .

By fitting single stellar population models to measured colors of the center of the lens galaxy, we estimated an *I*-band stellar mass-to-light ratio  $\Upsilon_{\star}$  from 2.8 to  $4.1 \Upsilon_{\odot,I}$ . Although a *constant* dark matter fraction of 20 per cent is thus not excluded, it is likely that dark matter does not play a significant role in the inner region of this early-type spiral galaxy of luminosity  $\sim L_{\star}$ . This is consistent with indications that less-luminous early-type galaxies (e.g. Gerhard et al. 2001; Rusin et al. 2003; Cappellari et al. 2006; Thomas et al. 2007; Bolton et al. 2008) and late-type galaxies (e.g. Persic et al. 1996; Palunas & Williams 2000; Bell & de Jong 2001; Kassin et al. 2006; Williams et al. 2009) are dominated by the stellar mass inside their central regions. This is different from dwarf galaxies as well as in (at least the outer parts of) giant elliptical and spiral galaxies where dark matter is expected to be ubiquitous.

The constraint  $\alpha = 1.0 \pm 0.1$  on the slope of the lens model implies that the intrinsic total mass density is close to isothermal, consistent with previous studies of lens galaxies (e.g. Koopmans et al. 2006, 2009). However, one has to be very careful not to over-interpret this result, not only due to assumptions in the modeling, but most of all because the slope is only (well) constrained around the Einstein radius  $R_E$ . If indeed mass follows light in the inner region of this lens galaxy, the (deprojected) surface brightness indicates deviations from isothermal towards the center where the slope becomes shallower as well as a possible steepening at larger radii. Interestingly, the construction of realistic galaxy density profiles with a stellar and dark matter component that are both non-isothermal, shows that the combined slope and corresponding lensing properties are nevertheless consistent with isothermal around  $R_E$  (van de Ven et al. 2009). With more extended images, e.g. in the case of galaxy-galaxy lensing, one can place a stronger constraint on the total mass distribution of the lens galaxy (e.g. Barnabè & Koopmans 2007; Suyu et al.

2009). Since the extension in these cases is still mostly tangential, constraining a large radial range is in particular possible when lensing occurs in multiple (redshift) planes, resulting in images at different Einstein radii (e.g. Gavazzi et al. 2008).

Nevertheless, already the quasar images provide an accurate constraint on the total mass within  $R_E$ , nearly independent of the details of the lens model (e.g. Kochanek 1991; Evans & Witt 2001). Therefore, at least around this radius no higher-order velocity moments are needed to break the mass-anisotropy degeneracy. Towards the center the surface brightness increases steeply, so that high enough S/N to measure velocity moments beyond  $V$  and  $\sigma$  might be achievable even at higher redshift. In the outer parts, the degeneracy might be (partially) broken by combining the kinematics of stars and/or discrete tracers, such as globular clusters and planetary nebulae, with total mass estimates from hot X-ray gas and/or weak lensing measurement (e.g. Gavazzi et al. 2007). In the current and even more in the upcoming extensive and deep photometric surveys, numerous (strong) gravitational lensing systems will be discovered. They provide important and independent constraints on the total mass distribution in galaxies, especially in combination with (resolved) stellar kinematics, as we showed in this paper (see also Barnabè & Koopmans 2007; Czoske et al. 2008; Barnabè et al. 2009).

We are grateful to Jean-René Roy and Matt Mountain for granting us director's discretionary time for this project and for generous hospitality in Hilo to TdZ. We thank Ed Turner for initial support of this project and Tracy Beck for efficient and cheerful assistance. We thank the referee for constructive comments on this work. GvdV acknowledges support provided by NASA through Hubble Fellowship grant HST-HF-01202.01-A awarded by the Space Telescope Science Institute, which is operated by the Association of Universities for Research in Astronomy, Inc., for NASA, under contract NAS 5-26555. MC acknowledges support from a STFC Advanced Fellowship (PP/D005574/1). Based on observations obtained at the Gemini Observatory, which is operated by the Association of Universities for Research in Astronomy, Inc., under a cooperative agreement with the NSF on behalf of the Gemini partnership: the National Science Foundation (United States), the Particle Physics and Astronomy Research Council (United Kingdom), the National Research Council (Canada), CONICYT (Chile), the Australian Research Council (Australia), CNPq (Brazil), and CONICET (Argentina).

## APPENDIX

### MULTI-GAUSSIAN EXPANSION

We summarize the (numerically) convenient expressions of the axisymmetric intrinsic density and gravitational potential in the case of a Multi-Gaussian Expansion (MGE) of the surface density (Monnet et al. 1992; Emsellem et al. 1994). Next, we show that also the gravitational lensing properties can be readily computed, so that the MGE method can be used to efficiently construct general lens models. Finally, we give the line-of-sight second-order velocity moment as a solution of the axisymmetric Jeans equations which is discussed in detail in Cappellari (2008).

*Axisymmetric density and potential*

We parameterize the surface brightness  $I(x', y')$  by a sum of Gaussian components

$$I_j(x', y') = I_{0,j} \exp \left\{ -\frac{1}{2\sigma_j'^2} \left[ x'^2 + \frac{y'^2}{q_j^2} \right] \right\}. \quad (\text{A1})$$

each with three parameters: the central surface brightness  $I_{0,j}$ , the dispersion  $\sigma_j'$  along the major  $x'$ -axis and the flattening  $q_j'$ . In case of an (oblate) axisymmetric system viewed at an inclination  $i > 0$ , the corresponding intrinsic luminosity density is

$$\nu_j(R, z) = \frac{q_j' I_{0,j}}{\sqrt{2\pi}\sigma_j q_j} \exp \left\{ -\frac{1}{2\sigma_j^2} \left[ R^2 + \frac{z^2}{q_j^2} \right] \right\}, \quad (\text{A2})$$

with intrinsic dispersion  $\sigma_j = \sigma_j'$  and intrinsic flattening  $q_j$  given by  $q_j^2 \sin^2 i = q_j'^2 - \cos^2 i$ .

The intrinsic mass density follows as  $\rho_j = \Upsilon_j \nu_j$ , where the mass-to-light ratio  $\Upsilon_j$  per Gaussian component is a free parameter. Alternatively, if the surface mass density  $\Sigma(x', y')$  is available (e.g. from gravitational lensing), an MGE-parameterization as in (A1) directly yields  $\rho_j$  as in (A2), but with  $I_{0,j}$  in both expressions replaced by the central surface mass density  $\Sigma_{0,j}$ .

The corresponding gravitational potential follows upon (numerical) evaluation of (Emsellem et al. 1994, eq. 39)

$$\Phi_j(R, z) = -\frac{2GM_j}{\sqrt{2\pi}\sigma_j} \int_0^1 \mathcal{F}_j(u) du, \quad (\text{A3})$$

where we have introduced

$$\mathcal{F}_j(u) = \exp \left\{ -\frac{u^2}{2\sigma_j^2} \left[ R^2 + \frac{z^2}{\mathcal{Q}_j^2(u)} \right] \right\} \frac{1}{\mathcal{Q}_j(u)}, \quad (\text{A4})$$

and  $\mathcal{Q}_j^2(u) = 1 - (1 - q_j^2) u^2$ . The total mass per Gaussian component is given by  $M_j = 2\pi\sigma_j'^2 q_j' \Sigma_{0,j}$ , with  $\Sigma_{0,j} = \Upsilon_j I_{0,j}$  when the mass density is inferred from the surface brightness.

In the latter case, we have implicitly assumed a *constant* mass-to-light ratio  $\Upsilon_j$  per Gaussian component by taking it outside the integral. Nevertheless, we can still mimic a (radially) varying mass-to-light ratio by considering the  $\Upsilon_j$  of the Gaussian components as free parameters (see e.g. van de Ven et al. 2006; van den Bosch et al. 2006). However, it is common in dynamical studies of the inner parts of galaxies (e.g. Cappellari et al. 2006) to assume the total mass-to-light ratio to be constant, i.e.,  $\Upsilon_j = \Upsilon_{\text{tot}}$  for each Gaussian component  $j$ . Since  $\Upsilon_{\text{tot}}$  may be larger than the stellar mass-to-light ratio  $\Upsilon_*$ , this still allows for possible dark matter contribution, but with a constant fraction.

*Axisymmetric lens model*

Under the thin-lens approximation, the gravitational lensing properties of a galaxy are characterized by the deflection potential  $\phi(x', y')$  and its (partial) derivatives. The deflection potential follows from projecting the potential along the line-of-sight or by solving the two-dimensional Poisson equation  $\nabla^2 \phi = 2\kappa$ . Here,  $\kappa = \Sigma/\Sigma_c$  is the normalized surface mass density with the critical lensing value  $\Sigma_c$  defined in equation (14).

Similar to the surface brightness in equation (A1), we parameterize this so-called ‘‘convergence’’  $\kappa(x', y')$  by a sum of Gaussian components

$$\kappa_k(x', y') = \frac{\Sigma_{0,k}}{\Sigma_c} \exp \left\{ -\frac{1}{2\sigma_k'^2} \left[ x'^2 + \frac{y'^2}{q_k^2} \right] \right\}. \quad (\text{A5})$$

The corresponding deflection potential is then

$$\phi_k(x', y') = -\frac{M_k}{\pi\Sigma_c} \int_0^1 \mathcal{F}_k'(u) \frac{du}{u}, \quad (\text{A6})$$

where  $M_k = 2\pi\sigma_k'^2 q_k' \Sigma_{0,k}$  is the total mass per Gaussian component, and we have introduced

$$\mathcal{F}_k'(u) = \exp \left\{ -\frac{u^2}{2\sigma_k'^2} \left[ x'^2 + \frac{y'^2}{\mathcal{Q}_k'^2(u)} \right] \right\} \frac{1}{\mathcal{Q}_k'(u)}, \quad (\text{A7})$$

and  $\mathcal{Q}_k'^2(u) = 1 - (1 - q_k'^2) u^2$ .

The first-order partial derivatives of  $\phi_k(x', y')$  follow as

$$\begin{aligned}\frac{\partial\phi_k}{\partial x'} &= x' \frac{M_k}{\pi\sigma_k'^2\Sigma_c} \int_0^1 \mathcal{F}'_k(u) u \, du, \\ \frac{\partial\phi_k}{\partial y'} &= y' \frac{M_k}{\pi\sigma_k'^2\Sigma_c} \int_0^1 \mathcal{F}'_k(u) \frac{u \, du}{\mathcal{Q}'_k{}^2(u)},\end{aligned}\tag{A8}$$

whereas the second-order partial derivatives are given by

$$\begin{aligned}\frac{\partial^2\phi_k}{\partial x'^2} &= \frac{M_k}{\pi\sigma_k'^2\Sigma_c} \int_0^1 \mathcal{F}'_k(u) \left[ 1 - \frac{x'^2}{\sigma_k'^2} u^2 \right] u \, du, \\ \frac{\partial^2\phi_k}{\partial y'^2} &= \frac{M_k}{\pi\sigma_k'^2\Sigma_c} \int_0^1 \mathcal{F}'_k(u) \left[ 1 - \frac{x'^2}{\sigma_k'^2} \frac{u^2}{\mathcal{Q}'_k{}^2(u)} \right] \frac{u \, du}{\mathcal{Q}'_k{}^2(u)}, \\ \frac{\partial^2\phi_k}{\partial x' \partial y'} &= \frac{M_k}{\pi\sigma_k'^2\Sigma_c} \int_0^1 \mathcal{F}'_k(u) \left[ \frac{x' y'}{\sigma_k'^2} u^2 \right] \frac{u \, du}{\mathcal{Q}'_k{}^2(u)}.\end{aligned}\tag{A9}$$

The above single integrals can be readily evaluated numerically, so that the lensing properties follow in a straightforward way. The image positions  $(x', y')$  are related to the source position  $(\xi, \eta)$  by the lens equation

$$\xi = x' - \sum_k \frac{\partial\phi_k}{\partial x'}, \quad \eta = y' - \sum_k \frac{\partial\phi_k}{\partial y'}.\tag{A10}$$

Given the parity  $p$  of the image, the magnification  $\mu$  is given by

$$\frac{1}{p\mu} = \left( 1 - \sum_k \frac{\partial^2\phi_k}{\partial x'^2} \right) \left( 1 - \sum_k \frac{\partial^2\phi_k}{\partial y'^2} \right) - \left( \sum_k \frac{\partial^2\phi_k}{\partial x' \partial y'} \right).\tag{A11}$$

The Einstein radius  $R_E$  follows from solving  $\bar{\kappa}(R_E) = 1$ , where  $\bar{\kappa}(R')$  is the average convergence within the projected radius  $R'$ . After substituting  $x' = R' \cos \theta'$  and  $y' = R' \sin \theta'$  in equation (A5) and performing the integral over  $R'$ , we are left with

$$\bar{\kappa}_k(R') = \frac{\sigma_k'^2 \Sigma_{0,k}}{\pi R'^2 \Sigma_c} \int_0^{2\pi} \left\{ 1 - \exp \left[ -\frac{R'^2 \mathcal{P}'(\theta')}{2\sigma_k'^2} \right] \right\} \frac{d\theta'}{\mathcal{P}'(\theta')},\tag{A12}$$

where  $\mathcal{P}'(\theta') = \cos^2 \theta' + \sin^2 \theta' / q_k'^2$ . The mass within the Einstein radius then follows as  $M_E = \Sigma_c \pi R_E^2$ .

#### Axisymmetric Jeans equations

We consider a luminous component with Gaussian intrinsic luminosity density  $\nu_j$  given by (A2), of which the observed kinematics trace the underlying gravitational potential  $\Phi = \sum_k \Phi_k$ , with the sum over all (luminous and dark) components  $\Phi_k$  given by (A3).

Assuming that the velocity ellipsoid is aligned with the cylindrical  $(R, \phi, z)$  coordinate system, so that  $\overline{v_R v_z} = 0$ , we can readily solve Jeans equation (2) as (Emsellem et al. 1994, eq. 42)

$$[\overline{v_z^2}]_j = 4\pi G \sum_k \frac{q_k' \Sigma_{0,k}}{\sqrt{2\pi} \sigma_k} \int_0^1 q_j^2 \sigma_j^2 \frac{\mathcal{F}_k(u) u^2}{1 - F_{jk} u^2} \, du,\tag{A13}$$

with  $\mathcal{F}_k(u)$  defined in (A4) and

$$F_{jk} = 1 - q_k^2 - q_j^2 \sigma_j^2 / \sigma_k^2.\tag{A14}$$

If we next also assume a constant flattening of the velocity ellipsoid in the meridional plane, we can write  $[\overline{v_R^2}]_j = b_j [\overline{v_z^2}]_j$ , and solve Jeans equation (1) as

$$[\overline{v_\phi^2}]_j = 4\pi G \sum_k \frac{q_k' \Sigma_{0,k}}{\sqrt{2\pi} \sigma_k} \int_0^1 [b_j q_j^2 \sigma_j^2 + \mathcal{G}_{jk}(u) R^2] \frac{\mathcal{F}_k(u) u^2}{1 - F_{jk} u^2} \, du,\tag{A15}$$

where we have introduced

$$\mathcal{G}_{jk}(u) = 1 - b_j q_j^2 - [b_j(1 - q_k^2) + (1 - b_j) F_{jk}] u^2.\tag{A16}$$

Since the constant  $b_j$  may be different for each luminous component  $j$ , the total anisotropy in the meridional plane

$$\beta_Z = 1 - \frac{\overline{v_z^2}}{v_R^2} = 1 - \frac{\sum_j \nu_j [\overline{v_z^2}]_j}{\sum_j b_j \nu_j [\overline{v_z^2}]_j},\tag{A17}$$

is allowed to vary throughout the system. In case of isotropy in the meridional plane all  $b_j = 1$  and thus  $\beta_Z = 0$ , corresponding to a two-integral DF  $f(E, L_z)$  (Emsellem et al. 1994).

After substitution of these expressions in equation (3), the line-of-sight integral can be solved, resulting in (Cappellari 2008, eq. 28)

$$\overline{[v_{\text{los}}^2]_j} = \frac{4\pi^{3/2}G}{I_j(x', y')} \frac{q'_j I_{0,j}}{\sqrt{2\pi}\sigma_j q_j} \sum_k \frac{q'_k \Sigma_{0,k}}{\sqrt{2\pi}\sigma_k} \int_0^1 \frac{q_j^2 \sigma_j^2 (\cos^2 i + b_j \sin^2 i) + \mathcal{G}_{jk}(u) x'^2 \sin^2 i}{(1 - F_{jk} u^2) \sqrt{[1 - (1 - q_k^2) u^2] (\mathcal{A} + \mathcal{B} \cos^2 i)}} \times u^2 \exp \left\{ -\mathcal{A} \left[ x'^2 + \frac{(\mathcal{A} + \mathcal{B}) y'^2}{\mathcal{A} + \mathcal{B} \cos^2 i} \right] \right\} du, \quad (\text{A18})$$

where  $\mathcal{A}$  and  $\mathcal{B}$  are functions of  $u$  defined as

$$\mathcal{A} = \frac{1}{2} \left( \frac{1}{\sigma_j^2} + \frac{u^2}{\sigma_k^2} \right), \quad (\text{A19})$$

$$\mathcal{B} = \frac{1}{2} \left( \frac{1 - q_j^2}{q_j^2 \sigma_j^2} + \frac{(1 - q_k^2) u^4}{[1 - (1 - q_k^2) u^2] \sigma_k^2} \right). \quad (\text{A20})$$

The remaining single integral can be readily evaluated numerically.

This provides a direct prediction of the combination  $V^2 + \sigma^2$  of the observed mean line-of-sight velocity  $V$  and dispersion  $\sigma$  at a given position  $(x', y')$  on the sky-plane, through the (luminosity weighted) sum  $\overline{v_{\text{los}}^2}(x', y') = \sum_j I_j \overline{[v_{\text{los}}^2]_j} / \sum_j I_j$  over the corresponding luminous components.

#### REFERENCES

- Agol, E., Jones, B., & Blaes, O. 2000, *ApJ*, 545, 657  
 Barnabè, M., Czoske, O., Koopmans, L. V. E., Treu, T., Bolton, A. S., & Gavazzi, R. 2009, *MNRAS*, 399, 21  
 Barnabè, M. & Koopmans, L. V. E. 2007, *ApJ*, 666, 726  
 Barnes, D. G., Webster, R. L., Schmidt, R. W., & Hughes, A. 1999, *MNRAS*, 309, 641  
 Bell, E. F. & de Jong, R. S. 2001, *ApJ*, 550, 212  
 Binney, J. & Merrifield, M. 1998, *Galactic astronomy* (Princeton, NJ, Princeton University Press)  
 Binney, J. & Tremaine, S. 1987, *Galactic Dynamics* (Princeton, NJ, Princeton University Press)  
 Blanton, M., Turner, E. L., & Wambsganss, J. 1998, *MNRAS*, 298, 1223  
 Bolton, A. S., Treu, T., Koopmans, L. V. E., Gavazzi, R., Moustakas, L. A., Burles, S., Schlegel, D. J., & Wayth, R. 2008, *ApJ*, 684, 248  
 Cappellari, M. 2002, *MNRAS*, 333, 400  
 —. 2008, *MNRAS*, 390, 71  
 Cappellari, M., Bacon, R., Bureau, M., Damen, M. C., Davies, R. L., de Zeeuw, P. T., Emsellem, E., Falcón-Barroso, J., Krajnović, D., Kuntschner, H., McDermid, R. M., Peletier, R. F., Sarzi, M., van den Bosch, R. C. E., & van de Ven, G. 2006, *MNRAS*, 366, 1126  
 Cappellari, M. & Copin, Y. 2003, *MNRAS*, 342, 345  
 Cappellari, M. & Emsellem, E. 2004, *PASP*, 116, 138  
 Carollo, C. M., de Zeeuw, P. T., van der Marel, R. P., Danziger, I. J., & Qian, E. E. 1995, *ApJ*, 441, L25  
 Chae, K.-H., Turnshek, D. A., & Khersonsky, V. K. 1998, *ApJ*, 495, 609  
 Côté, P., McLaughlin, D. E., Cohen, J. G., & Blakeslee, J. P. 2003, *ApJ*, 591, 850  
 Czoske, O., Barnabè, M., Koopmans, L. V. E., Treu, T., & Bolton, A. S. 2008, *MNRAS*, 384, 987  
 Dai, X., Chartas, G., Agol, E., Bautz, M. W., & Garmire, G. P. 2003, *ApJ*, 589, 100  
 de Jong, R. S. & Bell, E. F. 2007, *Comparing Dynamical and Stellar Population Mass-To-Light Ratio Estimates* (Island Universes - Structure and Evolution of Disk Galaxies), 107  
 Dejonghe, H. 1987, *MNRAS*, 224, 13  
 Dolphin, A. E. 2000, *PASP*, 112, 1397  
 Emsellem, E., Monnet, G., & Bacon, R. 1994, *A&A*, 285, 723  
 Evans, N. W. & Witt, H. J. 2001, *MNRAS*, 327, 1260  
 —. 2003, *MNRAS*, 345, 1351  
 Falco, E. E., Lehar, J., Perley, R. A., Wambsganss, J., & Gorenstein, M. V. 1996, *AJ*, 112, 897  
 Fitte, C. & Adam, G. 1994, *A&A*, 282, 11  
 Foltz, C. B., Hewett, P. C., Webster, R. L., & Lewis, G. F. 1992, *ApJ*, 386, L43  
 Franx, M., van Gorkom, J. H., & de Zeeuw, T. 1994, *ApJ*, 436, 642  
 Fukazawa, Y., Botoya-Nonesca, J. G., Pu, J., Ohto, A., & Kawano, N. 2006, *ApJ*, 636, 698  
 Gavazzi, R., Treu, T., Koopmans, L. V. E., Bolton, A. S., Moustakas, L. A., Burles, S., & Marshall, P. J. 2008, *ApJ*, 677, 1046  
 Gavazzi, R., Treu, T., Rhodes, J. D., Koopmans, L. V. E., Bolton, A. S., Burles, S., Massey, R. J., & Moustakas, L. A. 2007, *ApJ*, 667, 176  
 Gebhardt, K., Richstone, D., Tremaine, S., Lauer, T. R., Bender, R., Bower, G., Dressler, A., Faber, S. M., Filippenko, A. V., Green, R., Grillmair, C., Ho, L. C., Kormendy, J., Magorrian, J., & Pinkney, J. 2003, *ApJ*, 583, 92  
 Gerhard, O., Kronawitter, A., Saglia, R. P., & Bender, R. 2001, *AJ*, 121, 1936  
 Gerhard, O. E. 1993, *MNRAS*, 265, 213  
 Hook, I. M., Jørgensen, I., Allington-Smith, J. R., Davies, R. L., Metcalfe, N., Murowinski, R. G., & Crampton, D. 2004, *PASP*, 116, 425  
 Huchra, J., Gorenstein, M., Kent, S., Shapiro, I., Smith, G., Horine, E., & Perley, R. 1985, *AJ*, 90, 691  
 Humphrey, P. J. & Buote, D. A. 2010, *MNRAS*, 403, 2143  
 Hunter, C. 1977, *AJ*, 82, 271  
 Irwin, M. J., Webster, R. L., Hewett, P. C., Corrigan, R. T., & Jedrzejewski, R. I. 1989, *AJ*, 98, 1989  
 Jeans, J. H. 1915, *MNRAS*, 76, 70  
 Kassin, S. A., de Jong, R. S., & Weiner, B. J. 2006, *ApJ*, 643, 804  
 Kauffmann, G. & van den Bosch, F. 2002, *Scientific American*, 286, 36  
 Keeton, C. R. 2001, *ArXiv Astrophysics e-prints*, (arXiv:astro-ph/0102340)  
 Kent, S. M. & Falco, E. E. 1988, *AJ*, 96, 1570  
 Kochanek, C. S. 1991, *ApJ*, 373, 354  
 Kochanek, C. S., Falco, E. E., Impey, C. D., Lehar, J., McLeod, B. A., Rix, H.-W., Keeton, C. R., Muñoz, J. A., & Peng, C. Y. 2000, *ApJ*, 543, 131  
 Koopmans, L. V. E., Bolton, A., Treu, T., Czoske, O., Auger, M. W., Barnabè, M., Vegetti, S., Gavazzi, R., Moustakas, L. A., & Burles, S. 2009, *ApJ*, 703, L51  
 Koopmans, L. V. E. & Treu, T. 2003, *ApJ*, 583, 606

- Koopmans, L. V. E., Treu, T., Bolton, A. S., Burles, S., & Moustakas, L. A. 2006, *ApJ*, 649, 599
- Krist, J. & Hook, R. 2004, *The Tiny Tim User's Guide (v6.3)*
- Kroupa, P. 2001, *MNRAS*, 322, 231
- Lambas, D. G., Maddox, S. J., & Loveday, J. 1992, *MNRAS*, 258, 404
- Lynden-Bell, D. 1962, *MNRAS*, 123, 447
- Maraston, C. 1998, *MNRAS*, 300, 872
- . 2005, *MNRAS*, 362, 799
- Mediavilla, E., Arribas, S., del Burgo, C., Oscoz, A., Serra-Ricart, M., Alcalde, D., Falco, E. E., Goicoechea, L. J., Garcia-Lorenzo, B., & Buitrago, J. 1998, *ApJ*, 503, L27
- Merritt, D., Navarro, J. F., Ludlow, A., & Jenkins, A. 2005, *ApJ*, 624, L85
- Metcalf, R. B., Moustakas, L. A., Bunker, A. J., & Parry, I. R. 2004, *ApJ*, 607, 43
- Monnet, G., Bacon, R., & Emsellem, E. 1992, *A&A*, 253, 366
- Morganti, R., Sadler, E. M., Oosterloo, T., Pizzella, A., & Bertola, F. 1997, *AJ*, 113, 937
- Murray, G. J., Allington-Smith, J. R., Content, R., Davies, R. L., Dodsworth, G. N., Miller, B., Jorgensen, I., Hook, I., Crampton, D., & Murowinski, R. G. 2003, *SPIE*, 4841, 1750
- Navarro, J. F., Frenk, C. S., & White, S. D. M. 1997, *ApJ*, 490, 493
- Palunas, P. & Williams, T. B. 2000, *AJ*, 120, 2884
- Persic, M., Salucci, P., & Stel, F. 1996, *MNRAS*, 281, 27
- Primack, J. R. 2004, in *IAU Symp. 220: Dark Matter in Galaxies*, eds. S. D. Ryder, D. J. Pisano, M. A. Walker, and K. C. Freeman, 53
- Racine, R. 1991, *AJ*, 102, 454
- Rix, H.-W., de Zeeuw, P. T., Cretton, N., van der Marel, R. P., & Carollo, C. M. 1997, *ApJ*, 488, 702
- Rix, H.-W., Schneider, D. P., & Bahcall, J. N. 1992, *AJ*, 104, 959
- Rix, H.-W. & White, S. D. M. 1992, *MNRAS*, 254, 389
- Romanowsky, A. J., Douglas, N. G., Arnaboldi, M., Kuijken, K., Merrifield, M. R., Napolitano, N. R., Capaccioli, M., & Freeman, K. C. 2003, *Science*, 301, 1696
- Rusin, D., Kochanek, C. S., & Keeton, C. R. 2003, *ApJ*, 595, 29
- Salpeter, E. E. 1955, *ApJ*, 121, 161
- Schlegel, D. J., Finkbeiner, D. P., & Davis, M. 1998, *ApJ*, 500, 525
- Schmidt, R., Webster, R. L., & Lewis, G. F. 1998, *MNRAS*, 295, 488
- Schneider, P., Ehlers, J., & Falco, E. E. 1992, *Gravitational Lenses* (Springer-Verlag Berlin Heidelberg New York)
- Schwarzschild, M. 1979, *ApJ*, 232, 236
- Spergel, D. N., Bean, R., Doré, O., Nolta, M. R., Bennett, C. L., Dunkley, J., Hinshaw, G., Jarosik, N., Komatsu, E., Page, L., Peiris, H. V., Verde, L., Halpern, M., Hill, R. S., Kogut, A., Limon, M., Meyer, S. S., Odegard, N., Tucker, G. S., Weiland, J. L., Wollack, E., & Wright, E. L. 2007, *ApJS*, 170, 377
- Suyu, S. H., Marshall, P. J., Blandford, R. D., Fassnacht, C. D., Koopmans, L. V. E., McKean, J. P., & Treu, T. 2009, *ApJ*, 691, 277
- Thomas, J., Saglia, R. P., Bender, R., Thomas, D., Gebhardt, K., Magorrian, J., Corsini, E. M., & Wegner, G. 2007, *MNRAS*, 382, 657
- Tremaine, S., Gebhardt, K., Bender, R., Bower, G., Dressler, A., Faber, S. M., Filippenko, A. V., Green, R., Grillmair, C., Ho, L. C., Kormendy, J., Lauer, T. R., Magorrian, J., Pinkney, J., & Richstone, D. 2002, *ApJ*, 574, 740
- Treu, T. & Koopmans, L. V. E. 2004, *ApJ*, 611, 739
- Trott, C. M. & Webster, R. L. 2002, *MNRAS*, 334, 621
- Valluri, M., Merritt, D., & Emsellem, E. 2004, *ApJ*, 602, 66
- van Albada, T. S., Bahcall, J. N., Begeman, K., & Sancisi, R. 1985, *ApJ*, 295, 305
- van de Ven, G., de Zeeuw, P. T., & van den Bosch, R. C. E. 2008, *MNRAS*, 385, 614
- van de Ven, G., Mandelbaum, R., & Keeton, C. R. 2009, *MNRAS*, 398, 607
- van de Ven, G., van den Bosch, R. C. E., Verolme, E. K., & de Zeeuw, P. T. 2006, *A&A*, 445, 513
- van de Ven, G., van Dokkum, P. G., & Franx, M. 2003, *MNRAS*, 344, 924
- van den Bosch, R., de Zeeuw, T., Gebhardt, K., Noyola, E., & van de Ven, G. 2006, *ApJ*, 641, 852
- van den Bosch, R. C. E., van de Ven, G., Verolme, E. K., Cappellari, M., & de Zeeuw, P. T. 2008, *MNRAS*, 385, 647
- van der Marel, R. P. 1991, *MNRAS*, 253, 710
- van der Marel, R. P., Cretton, N., de Zeeuw, P. T., & Rix, H. 1998, *ApJ*, 493, 613
- van der Marel, R. P. & Franx, M. 1993, *ApJ*, 407, 525
- van Dokkum, P. G. 2001, *PASP*, 113, 1420
- Vazdekis, A., Casuso, E., Peletier, R. F., & Beckman, J. E. 1996, *ApJS*, 106, 307
- Vazdekis, A., Cenarro, A. J., Gorgas, J., Cardiel, N., & Peletier, R. F. 2003, *MNRAS*, 340, 1317
- Wambsganss, J. & Paczynski, B. 1994, *AJ*, 108, 1156
- Weijmans, A., Cappellari, M., Bacon, R., de Zeeuw, P. T., Emsellem, E., Falcón-Barroso, J., Kuntschner, H., McDermid, R. M., van den Bosch, R. C. E., & van de Ven, G. 2009, *MNRAS*, 398, 561
- Weijmans, A.-M., Krajnović, D., van de Ven, G., Oosterloo, T. A., Morganti, R., & de Zeeuw, P. T. 2008, *MNRAS*, 383, 1343
- Williams, M. J., Bureau, M., & Cappellari, M. 2009, *MNRAS*, 400, 1665
- Yee, H. K. C. 1988, *AJ*, 95, 1331